A Fourier-series-based Virtual Fields Method for the identification of 3-D stiffness distributions and its application to incompressible materials

TT Nguyen[1,2], JM Huntley[1], IA Ashcroft[3], PD Ruiz[1] and F Pierron[4]

[1] *Loughborough University, Wolfson School of Mechanical, Manufacturing and Electrical Engineering, Loughborough LE11 3TU, UK*

[2] *Current address: London South Bank Innovation Centre, TWI Ltd., Granta Park, Great Abington, Cambridge CB21 6AL, UK*

[3] *University of Nottingham, Faculty of Engineering, Nottingham NG7 2RD, UK*

[4] *University of Southampton, Faculty of Engineering and the Environment, Highfield, Southampton SO17 1BJ, UK*

Abstract:

We present an inverse method to identify the spatially-varying stiffness distributions in three-dimensions (3-D). The method is an extension of the classical Virtual Fields Method (VFM) – a numerical technique which exploits information from full-field deformation measurements to deduce unknown material properties – in the spatial frequency domain, which we name the Fourier-series-based Virtual Fields Method (F-VFM). Three-dimensional stiffness distributions, parameterised by a Fourier series expansion, are recovered after a single matrix inversion. A numerically efficient version of the technique is developed, based on the Fast Fourier Transform. The proposed F-VFM is also adapted to deal with the challenging situation of limited or even non-existent knowledge of boundary conditions. The 3-D F-VFM is validated with both numerical and experimental data. The latter came from a phase contrast MRI experiment containing material with Poisson's ratio close to 0.5; such a case requires a slightly different interpretation of the F-VFM equations, to enable the application of the technique to incompressible materials.

Keywords:

Stiffness identification, virtual fields method, Fourier series, unspecified boundary conditions, incompressible materials

1. Introduction

A typical characteristic of common diseases in the human body such as kidney stones or tumours is the presence of a hard mineral deposit or a solid stiff mass of pathological tissue within surrounding soft organs. Ultrasonography [1, 2] and magnetic resonance imaging (MRI) [3, 4] can be used to detect such inclusions non-invasively. Qualitative detection can often be achieved by relying on natural contrast within the scanned images or volumes, followed by segmentation of the pathological regions of the tissues from the others. Quantitative detection by mapping the distribution of material stiffness, on the other hand, allows for better characterisation, and therefore potential treatment, of the pathology. It does, however, require further analysis of these scanned images to extract strain data. Data from dynamic experiments can be used with a direct inversion to solve for unknown shear modulus distributions [5], which is not usually possible with static data; a map of static strain data can give topographical information of the unknown shear modulus distribution and of the interfaces between different phases of the tissue at the same time [6], allowing the modulus recovery independent of the boundary conditions.

Biological tissues are generally considered as nearly incompressible materials [7]; quantitative characterisation of this type of material therefore concerns the distribution of its shear modulus. There exist in the literature different strategies to reconstruct spatially-varying modulus distributions of materials in general, and those of incompressible materials in particular. A direct method of inverting the elasto-static equilibrium equation for the modulus distributions was first published by Skovoroda et al. [8], and the uniqueness of the solution in 2-D was examined in [9]. The principle of the method is based on mathematical transformation of the equilibrium equation whilst also satisfying compatibility and continuity conditions to establish a partial differential equation, with the modulus being the unknown variable. Barbone et al. [10] approached the direct method from another direction which requires computation of the hydrostatic pressure gradients. Recently, Sinkus et al. [11] proposed an alternative approach to eliminate the hydrostatic pressure term by applying a curl operator to the acoustic wave propagation equation. The approach, however, needs third-order derivatives of the measured data and knowledge of local property parameters. An alternative technique, the finite element model updating method (see for example [12]) which minimizes the difference between the output of an experiment and its corresponding numerical simulation, is superficially attractive because it builds on sophisticated commercial

codes thus reducing development time. However, it has at least two drawbacks: firstly the link between the uncertainty in the measurements and the uncertainty in recovered parameters is not explicit, and secondly the fact that it is inherently an iterative algorithm makes run times very long in three dimensions. Recent work on reconstructing distributions of elastic parameters of materials are presented in [13] where the determination of local stress fields in sub regions across the global domain based on full-field deformation data allowed for subsequent computations of constitutive parameters. The local stress distributions were implemented through a parameterisation of Airy stress potentials using Fourier series.

The virtual fields method (VFM) is a different approach, which is able to recover modulus distributions inside a material from its measured deformation data without any iterative calculation [14]. One drawback of the VFM is the need for spatial first derivatives of displacements, which amplifies the effect of measurement noise in the final results [15]. The first application of the VFM to modulus reconstruction of materials in 3-D has been presented in [16] in which the equilibrium equations are discretised by finite element 'shape functions'. A wise choice of the virtual fields eliminates the unknown hydrostatic pressure and its gradients by zeroing the tractions on the boundary. A detailed theory of the VFM can be found in [14]. The technique was recently adapted to Magnetic Resonance Elastography data [17] using a sliding window of 64 virtual elements which have been optimised with respect to noise sensitivity following the approach in [15].

In this paper, we retain the basic concepts underlying the VFM in statics, but approach the parameterisation of the unknown modulus distribution in the spatial frequency domain by performing a 3-D Fourier series expansion over the region of interest. Virtual fields are not selected as polynomials of spatial variables, as in the classical VFM literature, but from a set of simple cosine or sine functions of different spatial frequencies. The abbreviation F-VFM will be used to denote the VFM in which Fourier series are used in the parameterisation of the modulus and for the virtual fields.

The F-VFM was developed originally for 2-D geometries in [18] and extended in [19] to the case of incomplete knowledge of the boundary value distributions. In the current paper, it is extended for the first time to volumetric data resulting from, for example, measurements with Digital Volume Correlation or phase contrast Magnetic Resonance Imaging (MRI). The main part of the paper (Section 2) includes the theoretical development of the F-VFM in 3-D and its fast algorithm. Section 3 shows the results of applying the 3-D F-VFM to one numerical

and one experimental scenario, and Section 4 summarises the key outcomes of the proposed technique.

2. Implementation of the F-VFM in 3-D

2.1. Principles of the F-VFM

2.1.1. Parameterisation of non-uniform stiffness

The fundamental equation of the F-VFM is derived from the principle of virtual work (PVW) equation (integral form) written for a deformable body, which describes the balance between the virtual works of internal and external forces with any continuous and differentiable virtual displacement field (and its associated virtual strain field). In the case of a static body where the body force is small enough to be neglected, the equilibrium equation of the body can be written as in [14]:

$$-\int_{V} \boldsymbol{\sigma}: \boldsymbol{\epsilon}^{*}\, dV + \int_{S_f} \mathbf{T}\mathbf{u}^{*} dS_f = 0 \tag{1}$$

The equation represents a quasi-static equilibrium state of the deformable body subjected to surface forces, which are represented by the traction vector **T** or the density of surface forces acting on a small surface element dS_f. As the body force is neglected, the surface forces are commonly called external forces. The (second-order) Cauchy stress tensor **σ** in the equation represents the internal forces that oppose the external forces. The equilibrium equation (1) is then established by multiplying these (internal and external) forces by virtual quantities to build up the so-called virtual work equations. The virtual quantities, those with superscript '*' throughout the paper, can be either a virtual displacement vector $\mathbf{u}^{*}$ or a virtual strain tensor $\boldsymbol{\epsilon}^{*}$ whose components are tailored to derive specific equations to solve particular problems, and will be discussed in more detail in the next section.

Consider now a cuboidal volume *V* of global dimensions L_x, L_y and L_z along the Cartesian *x*, *y* and *z* axes, respectively (see Fig. 1), containing a material with a linear elastic response to the applied forces. Column vector **σ** (we use the same notation as for the related stress tensor for simplicity) of length 6×1 in Eq. (1) containing six components of the Cauchy stress tensor by adopting Voigt's notation, can be expressed as a product of the stiffness matrix **Q** and the vector **ϵ** containing components of strain tensor according to the constitutive relation of the material, resulting in a more explicit form of this equation as

$$\int_V \boldsymbol{\epsilon}^* \mathbf{Q} \boldsymbol{\epsilon}\, dV = \int_{S_f} \mathbf{T}\mathbf{u}^* dS_f \tag{2}$$

We now restrict our attention to the case of isotropic materials, for which the stiffness matrix **Q** is only dependent on two elastic parameters *E* (elastic modulus) and *v* (Poisson's ratio) as follows

$$\mathbf{Q} = \begin{pmatrix} 1 & \frac{\nu}{1-\nu} & \frac{\nu}{1-\nu} & 0 & 0 & 0 \\ \frac{\nu}{1-\nu} & 1 & \frac{\nu}{1-\nu} & 0 & 0 & 0 \\ \frac{\nu}{1-\nu} & \frac{\nu}{1-\nu} & 1 & 0 & 0 & 0 \\ 0 & 0 & 0 & \frac{1-2\nu}{2(1-\nu)} & 0 & 0 \\ 0 & 0 & 0 & 0 & \frac{1-2\nu}{2(1-\nu)} & 0 \\ 0 & 0 & 0 & 0 & 0 & \frac{1-2\nu}{2(1-\nu)} \end{pmatrix} Q_{xx} \tag{3}$$

with Q_{xx} related to *E* and *v* by the equation

$$Q_{xx} = \frac{E(1-\nu)}{(1+\nu)(1-2\nu)} \tag{4}$$

The substitution of Eq. (3) into Eq. (2) gives

$$\int_V \begin{pmatrix} \epsilon_{xx}^* \\ \epsilon_{yy}^* \\ \epsilon_{zz}^* \\ \gamma_{yz}^* \\ \gamma_{zx}^* \\ \gamma_{xy}^* \end{pmatrix}' \begin{pmatrix} 1 & \frac{\nu}{1-\nu} & \frac{\nu}{1-\nu} & 0 & 0 & 0 \\ \frac{\nu}{1-\nu} & 1 & \frac{\nu}{1-\nu} & 0 & 0 & 0 \\ \frac{\nu}{1-\nu} & \frac{\nu}{1-\nu} & 1 & 0 & 0 & 0 \\ 0 & 0 & 0 & \frac{1-2\nu}{2(1-\nu)} & 0 & 0 \\ 0 & 0 & 0 & 0 & \frac{1-2\nu}{2(1-\nu)} & 0 \\ 0 & 0 & 0 & 0 & 0 & \frac{1-2\nu}{2(1-\nu)} \end{pmatrix} \begin{pmatrix} \epsilon_{xx} \\ \epsilon_{yy} \\ \epsilon_{zz} \\ \gamma_{yz} \\ \gamma_{zx} \\ \gamma_{xy} \end{pmatrix} Q_{xx} dV \tag{5}$$

$$= \int_{S_f} \begin{pmatrix} T_x & T_y & T_z \end{pmatrix} \begin{pmatrix} u_x^* \\ u_y^* \\ u_z^* \end{pmatrix} dS_f$$

where $\epsilon_{\alpha\alpha}$ and $\gamma_{\alpha\beta}$ ($\alpha, \beta = x, y, z$), represent the normal and shear strain components, respectively, and superscript '*' denotes the corresponding virtual strain components. This can be written in non-matrix form as

$$\int_V P(x,y,z) Q_{xx} dV = \int_{S_f} \left(T_x u_x^* + T_y u_y^* + T_z u_z^* \right) dS_f \tag{6}$$

with

$$\begin{aligned} P(x,y,z) = P = & \left(\epsilon_{xx} + \frac{\nu}{1-\nu} \left(\epsilon_{yy} + \epsilon_{zz} \right) \right) \epsilon_{xx}^* \\ & + \left(\epsilon_{yy} + \frac{\nu}{1-\nu} \left(\epsilon_{xx} + \epsilon_{zz} \right) \right) \epsilon_{yy}^* \\ & + \left(\epsilon_{zz} + \frac{\nu}{1-\nu} \left(\epsilon_{xx} + \epsilon_{yy} \right) \right) \epsilon_{zz}^* + \frac{1-2\nu}{2(1-\nu)} \left(\gamma_{yz} \gamma_{yz}^* + \gamma_{zx} \gamma_{zx}^* + \gamma_{xy} \gamma_{xy}^* \right) \end{aligned} \tag{7}$$

Earlier developments of the VFM relied on the assumption that the stiffness distribution, i.e. Q_{xx} in Eq. (6), is uniform over the domain, allowing it to be taken out of the left-hand-side integral of this equation as a scalar constant. The integrand then only includes the measured and virtual deformation fields, which leads to a direct calculation of the stiffness [20], provided that the traction components in the right-hand-side integral are specified. The simplification of Q_{xx} as a scalar constant is only acceptable in macro-scale observations where materials are considered homogeneous. At meso- and micro-scales however, materials are no longer homogeneous. A parameterisation of the stiffness may therefore be necessary. The first attempts to parameterise the stiffness as a collection of polynomials have been described in [21] in which unknown coefficients of the polynomials were gathered in an unknown vector, then isolated from the integral and computed by a single matrix inversion operation. Recently, a discrete (piece-wise) parameterisation algorithm of the VFM has been proposed and successfully applied in 2-D [22], 3-D [16] and to welds [23-25]. 2-D parameterisation of the F-VFM was presented in detail in [18] and is extended here to 3-D.

In the simplest form where v is approximated as a known position-independent constant[1], Q_{xx} may be written as follows:

$$Q_{xx}(x,y,z) = \sum_{m=0}^{M}\sum_{n=-N}^{N}\sum_{o=-O}^{O} a_{m,n,o}\cos 2\pi\left(\frac{mx}{L_x}+\frac{ny}{L_y}+\frac{oz}{L_z}\right) + \sum_{m=0^*}^{M}\sum_{n=-N^*}^{N}\sum_{o=-O^*}^{O} b_{m,n,o}\sin 2\pi\left(\frac{mx}{L_x}+\frac{ny}{L_y}+\frac{oz}{L_z}\right) \tag{8}$$

where $a_{m,n,o}$, $b_{m,n,o}$ are the Fourier coefficients of the series with non-dimensional spatial frequency components (m, n, o), and M, N, O are the maximum values of the indices m, n and o, respectively. The presence of negative frequency coefficients (n and o) in Eq. (8) needs a brief explanation. In a standard 3-D discrete Fourier transform, the lower limit for m, n and o would be 0. Negative frequencies in that case are implicitly present as aliased high frequencies generated by m, n and o values lying above the Nyquist limit. In the current case, however, the upper limit of m, n and o in practice will lie well below the Nyquist frequency for typical strain field resolutions. For example, for a 100×100×100 pixel strain field, we would require M, N and O to equal 100 before all the negative frequencies could be generated in this way. The number of degrees of freedom would then become impractically large and in practice, as will be seen in Section 3, we typically choose values of M, N and O less than 20. As a result, it is necessary to explicitly include the negative frequencies in the summation of Eq. (8). However, due to the even/ odd symmetry of the cosine/ sine functions, only two of the three indices m, n and o need to take negative values. In this case we have chosen index m to take the values from 0 to M whilst index n runs from $–N$ to N and o from $–O$ to O. This would reduce the number of required coefficients of the Fourier series by a factor of 2 compared to the situation where all indices were allowed to take negative values. Condition (*) for the indices of the sine part of Eq. (8) prevents the three indices from being zero at the same time, which otherwise would later lead to a zero row of the left-hand-side matrix.

[1] The assumption that v is a known constant is reasonable in many cases, but where it is not, a second Fourier series expansion of the variable vQ_{xx} can be performed. This leads to a second set of Fourier coefficients that need to be solved for as part of the analysis.

Eq. (8) can also be represented in matrix form with the use of shorthand notations for cosine and sine functions with spatial frequency components (m, n, o) as $c_{m,n,o} = c_{m,n,o}(x,y,z) = \cos 2\pi\left(\frac{mx}{L_x}+\frac{ny}{L_y}+\frac{oz}{L_z}\right)$ and $s_{m,n,o} = s_{m,n,o}(x,y,z) = \sin 2\pi\left(\frac{mx}{L_x}+\frac{ny}{L_y}+\frac{oz}{L_z}\right)$ so that

$$Q_{xx}(x,y,z) = \sum_{m=0}^{M}\sum_{n=-N}^{N}\sum_{o=-O}^{O} a_{m,n,o}c_{m,n,o}(x,y,z) + \sum_{m=0^*}^{M}\sum_{n=-N^*}^{N}\sum_{o=-O^*}^{O} b_{m,n,o}s_{m,n,o}(x,y,z) \tag{9}$$

or

$$Q_{xx}(x,y,z) = (1 \quad \dots c_{m,n,o}(x,y,z)\dots \quad \dots s_{m,n,o}(x,y,z)\dots)\begin{pmatrix} a_{0,0,0} \\ \vdots \\ a_{m,n,o} \\ \vdots \\ b_{m,n,o} \\ \vdots \end{pmatrix} \tag{10}$$

The substitution of Eq. (10) into Eq. (6) leads to an equation of the F-VFM associated with a single choice of the virtual fields as follows:

$$\left(\int_V P dV \quad \dots \int_V P c_{m,n,o} dV \dots \quad \dots \int_V P s_{m,n,o} dV \dots\right)\begin{pmatrix} a_{0,0,0} \\ \vdots \\ a_{m,n,o} \\ \vdots \\ b_{m,n,o} \\ \vdots \end{pmatrix} = \int_{S_f}\left(T_x u_x^* + T_y u_y^* + T_z u_z^*\right) dS_f \tag{11}$$

A particular choice of virtual field results in one equation of the form of Eq. (11). This one equation by itself is sufficient to obtain only the simplest solution of a single Fourier coefficient, the dc term $a_{0,0,0}$, corresponding to the case $m = n = o = 0$. However, additional equations are necessary to obtain the full set of Fourier coefficients by selecting different virtual fields, thus giving rise to different forms for the function $P(x, y, z)$. In what follows, $P^{(i)}(x,y,z)$ will be used to denote this function for the i-th virtual field, and so for the virtual displacements $u_\alpha^{*(i)}(\alpha = x,y,z)$. If we denote by N_F the total number of virtual fields sufficient to represent the unknown stiffness distribution, N_F independent equations of the

form of Eq. (11) are required. These equations can then be assembled to give the matrix equation:

$$\mathbf{MX} = \mathbf{Y} \tag{12}$$

in which

$$\mathbf{M} = \begin{pmatrix} \int_V P^{(1)} dV & \dots \int_V P^{(1)} c_{m,n,o} dV \dots & \dots \int_V P^{(1)} s_{m,n,o} dV \dots \\ \vdots & \vdots & \vdots \\ \int_V P^{(N_F)} dV & \dots \int_V P^{(N_F)} c_{m,n,o} dV \dots & \dots \int_V P^{(N_F)} s_{m,n,o} dV \dots \end{pmatrix} \tag{13}$$

$$\mathbf{X} = \begin{pmatrix} a_{0,0,0} \\ \vdots \\ a_{m,n,o} \\ \vdots \\ b_{m,n,o} \\ \vdots \end{pmatrix} \tag{14}$$

$$\mathbf{Y} = \begin{pmatrix} \int_{S_f} \left(T_x u_x^{*(1)} + T_y u_y^{*(1)} + T_z u_z^{*(1)} \right) dS_f \\ \vdots \\ \int_{S_f} \left(T_x u_x^{*(N_F)} + T_y u_y^{*(N_F)} + T_z u_z^{*(N_F)} \right) dS_f \end{pmatrix} \tag{15}$$

Eq. (12) is called the resolution matrix equation of the 3-D F-VFM as it will be inverted to solve for the vector **X** containing the desired Fourier coefficients $a_{m,n,o}$ and $b_{m,n,o}$ that describe the unknown stiffness distribution. The column vector **Y** contains distributions of traction components, with the number of its elements equal to N_F computed by

$$N_F = 2(M+1)(2N+1)(2O+1) - 1 \tag{16}$$

2.1.2. Selection of virtual displacement and strain fields

To find the coefficients of the stiffness Fourier series in Eq. (10), different virtual displacement fields and their derivatives are necessary to build up the left-hand-side matrix **M** defined in Eq. (13). The choice of these virtual fields is the key issue in any VFM application as it will directly affect the degree of independence of the matrix equation (12).

The VFM in its infancy witnessed the selection of potential virtual fields on a trial-and-error basis to ensure that the equations of the linear system (12) are independent. Later, the stability of the linear system was improved by means of a special virtual fields selection strategy [20]. Recent development of the VFM included an optimal selection of the virtual fields [15] which at the same time preserves the stability of the system of equations (12) and reduces the sensitivity of the method to noise. The virtual displacements and strains in those studies are defined as continuous functions either over the whole domain or piecewise within its subdomains. In the F-VFM, however, the virtual fields are chosen as an arrangement of simple cosine and sine functions of different frequencies. As Eq. (6) involves volume integrals of terms of the form $\epsilon^*_{\alpha\alpha}\epsilon_{\beta\beta}Q_{xx}$ ($\alpha, \beta = x, y, z$), the use of different spatial frequencies in the virtual fields therefore allows a given spatial frequency in the measured strain field $\epsilon_{\beta\beta}$ to be linked in turn with different coefficients in the Fourier expansion of Q_{xx}.

A few simple rules have been used to select the virtual fields as follows:

a) The set of virtual field spatial frequencies should be the same as that for the stiffness parameterisation so that a given spatial frequency in the measured strain field $\epsilon_{\beta\beta}$ can be linked in turn with all the coefficients in the Fourier expansion of Q_{xx};
b) Each spatial frequency for a given virtual strain field component should have both a sine and cosine wave of unit amplitude to ensure that the signal in $\epsilon_{\beta\beta}$ at that spatial frequency is detected regardless of its phase;
c) The total number of virtual fields should be equal to N_F in order to uniquely determine the unknown Fourier series coefficients in Eq. (12). Although the number of virtual fields can in principle be larger than N_F, the calculated Fourier series coefficients then represent a least squares solution of the matrix Eq. (12). If the number of virtual fields is less than N_F, no solution exists.

Specifically, the selection of the virtual fields was achieved by defining a set of virtual displacements u^*_x, u^*_y and u^*_z which then produce the six virtual strain fields simultaneously through differentiation. Thus, the virtual strain fields ϵ^*_{xx}, ϵ^*_{yy}, ϵ^*_{zz}, γ^*_{yz}, γ^*_{zx} and γ^*_{xy} consist of a set of cosine waves with spatial frequency components $p = 0..M$; $q = –N..N$, $r = –O..O$, giving $(M+1)(2N+1)(2O+1)$ independent virtual fields; and a set of corresponding sine waves in which the trivial case $p = q = r = 0$ is excluded, giving an additional $(M+1)(2N+1)(2O+1)$ –

1 fields. The total number of chosen cosine and sine virtual fields will therefore be equal to N_F, which is the required number to determine uniquely the unknown Fourier series coefficients of Eq. (10). An additional benefit resulting from this choice of virtual fields is that it allows a fast algorithm to be employed, based on 3-D fast Fourier transforms, as will be discussed in the next section.

The virtual displacements and their derivatives used in the 3-D F-VFM, including the special cases $p = 0$; $q = 0$ and $r = 0$, are summarized in Table 1. The virtual strains are then computed from these derivatives by

$$\begin{aligned} &\epsilon_{xx}^* = \frac{\partial u_x^*}{\partial x} \; ; \qquad \epsilon_{yy}^* = \frac{\partial u_y^*}{\partial y} \; ; \qquad \epsilon_{zz}^* = \frac{\partial u_z^*}{\partial z} \; ; \\ &\gamma_{yz}^* = \frac{\partial u_y^*}{\partial z} + \frac{\partial u_z^*}{\partial y} \; ; \qquad \gamma_{zx}^* = \frac{\partial u_z^*}{\partial x} + \frac{\partial u_x^*}{\partial z} \; ; \qquad \gamma_{xy}^* = \frac{\partial u_x^*}{\partial y} + \frac{\partial u_y^*}{\partial x} \end{aligned} \tag{17}$$

It is convenient to write matrix **M** of size $N_F \times N_F$ from Eq. (13) in terms of the sub-matrices **A**, **B**, **C** and **D** as follows:

$$\mathbf{M} = \begin{pmatrix} \mathbf{A} & \mathbf{B} \\ \mathbf{C} & \mathbf{D} \end{pmatrix} \tag{18}$$

where **A** is of size $(M+1)(2N+1)(2O+1)$ rows × $(M+1)(2N+1)(2O+1)$ columns, **B** is $(M+1)(2N+1)(2O+1)$ × $((M+1)(2N+1)(2O+1) - 1)$, **C** is $((M+1)(2N+1)(2O+1) - 1)$ × $(M+1)(2N+1)(2O+1)$, and **D** is $((M+1)(2N+1)(2O+1) - 1)$ × $((M+1)(2N+1)(2O+1) - 1)$. **A** and **C** contain the cosine terms $c_{m,n,o}$ in the stiffness expansion with **B** and **D** containing the sine terms $s_{m,n,o}$. **A** and **B** contain the corresponding cosine waves in $\epsilon_{\alpha\alpha}^*$ (denoted $c_{p,q,r}$) with **C** and **D** containing the sine terms $s_{p,q,r}$.

With the choice of virtual fields mentioned earlier, it is now possible to write the elements of matrix **M** in their explicit forms by combining Eq. (7), (17), Table 1 with Eq. (13). These representations will be useful when the fast algorithm of the F-VFM is introduced in the following section. The contribution of the experimental normal strains to the general element of matrix **M** can be expanded as

$$\int_V \left(\left(\epsilon_{xx} + \frac{\nu}{1-\nu}(\epsilon_{yy} + \epsilon_{zz}) \right) \epsilon_{xx}^* + \left(\epsilon_{yy} + \frac{\nu}{1-\nu}(\epsilon_{xx} + \epsilon_{zz}) \right) \epsilon_{yy}^* + \left(\epsilon_{zz} + \frac{\nu}{1-\nu}(\epsilon_{xx} + \epsilon_{yy}) \right) \epsilon_{zz}^* \right) \begin{Bmatrix} c_{m,n,o} \\ s_{m,n,o} \end{Bmatrix} dV = \frac{1+\nu}{1-\nu} \int_V (\epsilon_{xx} + \epsilon_{yy} + \epsilon_{zz}) \begin{Bmatrix} c_{p,q,r} \\ s_{p,q,r} \end{Bmatrix} \times \begin{Bmatrix} c_{m,n,o} \\ s_{m,n,o} \end{Bmatrix} dV \tag{19}$$

The $\begin{Bmatrix} \cdot \\ \cdot \end{Bmatrix} \times \begin{Bmatrix} \cdot \\ \cdot \end{Bmatrix}$ notation indicates a product of a cosine/sine virtual strain field component with a cosine/sine term from the stiffness expansion, the particular combination being dependent on the quadrant (**A**, **B**, **C** or **D**) of the matrix **M**, as defined in Eq. (18). Note that m, n, o are indices of the cosine/ sine terms from the stiffness expansion whilst p, q, r are those of the cosine/sine virtual strain fields. The shear strains involved in the formation of matrix **M** can be expressed in a similar way as follows:

$$\frac{1-2\nu}{2(1-\nu)} \int_V \gamma_{yz} \gamma_{yz}^* \begin{Bmatrix} c_{m,n,o} \\ s_{m,n,o} \end{Bmatrix} dV = \begin{cases} \frac{1-2\nu}{2(1-\nu)} \int_V \gamma_{yz} \left(\frac{L_y}{L_z} \frac{r}{q} + \frac{L_z}{L_y} \frac{q}{r} \right) \begin{Bmatrix} c_{p,q,r} \\ s_{p,q,r} \end{Bmatrix} \times \begin{Bmatrix} c_{m,n,o} \\ s_{m,n,o} \end{Bmatrix} dV \ \ (q \neq 0, r \neq 0) \\ \frac{1-2\nu}{2(1-\nu)} \int_V y \gamma_{yz} \left(\frac{2\pi r}{L_z} \right) \begin{Bmatrix} -s_{p,0,r} \\ c_{p,0,r} \end{Bmatrix} \times \begin{Bmatrix} c_{m,n,o} \\ s_{m,n,o} \end{Bmatrix} dV \ \ (q = 0) \\ \frac{1-2\nu}{2(1-\nu)} \int_V z \gamma_{yz} \left(\frac{2\pi q}{L_y} \right) \begin{Bmatrix} -s_{p,q,0} \\ c_{p,q,0} \end{Bmatrix} \times \begin{Bmatrix} c_{m,n,o} \\ s_{m,n,o} \end{Bmatrix} dV \ \ (r = 0) \end{cases} \tag{20}$$

$$\frac{1-2\nu}{2(1-\nu)} \int_V \gamma_{zx} \gamma_{zx}^* \begin{Bmatrix} c_{m,n,o} \\ s_{m,n,o} \end{Bmatrix} dV = \begin{cases} \frac{1-2\nu}{2(1-\nu)} \int_V \gamma_{zx} \left(\frac{L_x}{L_z} \frac{r}{p} + \frac{L_z}{L_x} \frac{p}{r} \right) \begin{Bmatrix} c_{p,q,r} \\ s_{p,q,r} \end{Bmatrix} \times \begin{Bmatrix} c_{m,n,o} \\ s_{m,n,o} \end{Bmatrix} dV \ \ (p \neq 0, r \neq 0) \\ \frac{1-2\nu}{2(1-\nu)} \int_V x \gamma_{zx} \left(\frac{2\pi r}{L_z} \right) \begin{Bmatrix} -s_{0,q,r} \\ c_{0,q,r} \end{Bmatrix} \times \begin{Bmatrix} c_{m,n,o} \\ s_{m,n,o} \end{Bmatrix} dV \ \ (p = 0) \\ \frac{1-2\nu}{2(1-\nu)} \int_V z \gamma_{zx} \left(\frac{2\pi p}{L_x} \right) \begin{Bmatrix} -s_{p,q,0} \\ c_{p,q,0} \end{Bmatrix} \times \begin{Bmatrix} c_{m,n,o} \\ s_{m,n,o} \end{Bmatrix} dV \ \ (r = 0) \end{cases} \tag{21}$$

$$\frac{1-2\nu}{2(1-\nu)}\int_V \gamma_{xy}\gamma_{xy}^{*}\begin{Bmatrix}c_{m,n,o}\\ s_{m,n,o}\end{Bmatrix}dV$$

$$=\begin{cases}\dfrac{1-2\nu}{2(1-\nu)}\displaystyle\int_V \gamma_{xy}\left(\frac{L_x}{L_y}\frac{q}{p}+\frac{L_y}{L_x}\frac{p}{q}\right)\begin{Bmatrix}c_{p,q,r}\\ s_{p,q,r}\end{Bmatrix}\times\begin{Bmatrix}c_{m,n,o}\\ s_{m,n,o}\end{Bmatrix}dV \ \ (p\neq 0, q\neq 0)\\ \dfrac{1-2\nu}{2(1-\nu)}\displaystyle\int_V x\gamma_{xy}\left(\frac{2\pi q}{L_y}\right)\begin{Bmatrix}-s_{0,q,r}\\ c_{0,q,r}\end{Bmatrix}\times\begin{Bmatrix}c_{m,n,o}\\ s_{m,n,o}\end{Bmatrix}dV \ \ (p=0)\\ \dfrac{1-2\nu}{2(1-\nu)}\displaystyle\int_V y\gamma_{xy}\left(\frac{2\pi p}{L_x}\right)\begin{Bmatrix}-s_{p,0,r}\\ c_{p,0,r}\end{Bmatrix}\times\begin{Bmatrix}c_{m,n,o}\\ s_{m,n,o}\end{Bmatrix}dV \ \ (q=0)\end{cases} \tag{22}$$

2.1.3. Fast F-VFM implementation

An efficient algorithm for the F-VFM using 3-D fast Fourier transforms (FFT) is presented in this section. Following the section above, the cross product $\begin{Bmatrix}\cdot\\ \cdot\end{Bmatrix}\times\begin{Bmatrix}\cdot\\ \cdot\end{Bmatrix}$ term from Eq. (19) to (22) can be rewritten in the following forms:

$$\begin{aligned}
c_{m,n,o}c_{p,q,r} &= \frac{1}{2}\left(c_{m+p,n+q,o+r}+c_{m-p,n-q,o-r}\right)\\
c_{m,n,o}s_{p,q,r} &= \frac{1}{2}\left(s_{m+p,n+q,o+r}-s_{m-p,n-q,o-r}\right)\\
s_{m,n,o}c_{p,q,r} &= \frac{1}{2}\left(s_{m+p,n+q,o+r}+s_{m-p,n-q,o-r}\right)\\
s_{m,n,o}s_{p,q,r} &= \frac{1}{2}\left(-c_{m+p,n+q,o+r}+c_{m-p,n-q,o-r}\right)
\end{aligned} \tag{23}$$

The right-hand sides of Eq. (19) to (22) all reduce to scaled versions of $\Re[H(j,k,l)]$ and $\Im[H(j,k,l)]$, respectively, where $\Re$ and $\Im$ denote real and imaginary parts of a complex variable, and H is given by

$$H(j,k,l)=\int_V h(x,y,z)(c_{j,k,l}-is_{j,k,l})dV \tag{24}$$

in which j, k and l are spatial frequency components, i is the square root of -1, and h is a function derived from the experimental strain fields. In discrete form, Eq. (24) can be written

$$H(j,k,l)\approx\frac{L_xL_yL_z}{N_xN_yN_z}\sum_{\bar{x}=0}^{N_x-1}\sum_{\bar{y}=0}^{N_y-1}\sum_{\bar{z}=0}^{N_z-1}\bar{h}(\bar{x},\bar{y},\bar{z})(\bar{c}_{j,k,l}-i\bar{s}_{j,k,l}) \tag{25}$$

where $\bar{x}$, $\bar{y}$ and $\bar{z}$ are non-dimensional spatial coordinates ($\bar{x} = 0,1,2,\ldots,N_x - 1;\ \bar{y} = 0,1,2,\ldots,N_y - 1;\ \bar{z} = 0,1,2,\ldots,N_z - 1$), $\bar{h}$ is h expressed in terms of these coordinates, and

$$\begin{aligned} \bar{c}_{j,k,l}(\bar{x},\bar{y},\bar{z}) &= \cos 2\pi\left(\frac{j\bar{x}}{N_x}+\frac{k\bar{y}}{N_y}+\frac{l\bar{z}}{N_z}\right) \\ \bar{s}_{j,k,l}(\bar{x},\bar{y},\bar{z}) &= \sin 2\pi\left(\frac{j\bar{x}}{N_x}+\frac{k\bar{y}}{N_y}+\frac{l\bar{z}}{N_z}\right) \end{aligned} \tag{26}$$

Eq. (25) is just the 3-D discrete Fourier transform of the sampled signal $\bar{h}(\bar{x},\bar{y},\bar{z})$ and can be calculated rapidly by a fast Fourier transform (FFT) algorithm, implemented for example as `fftn` in the MATLAB language. Spatial frequency components (*j*, *k*, *l*) have the same meaning in Eq. (25) and (26) as for the corresponding continuous form expressions $c_{j,k,l}$ and $s_{j,k,l}$, with units of 'cycles per field of view'. One assumption implicit in the use of the 3-D FFT is that the origin of the domain is at the bottom left of the field of view. The shift of the origin to the centroid of the volume of interest, as for the application considered in the next section, can be achieved by swapping the quadrants of the experimental strain fields along each direction, for example with the MATLAB `fftshift` function.

A total of 10 FFTs of the function *h* in the right-hand sides of Eq. (19) to (22) are required to build up matrix **M**, which are shown as follows:

$$\begin{aligned} h_1(x,y,z) &= \epsilon_{xx}(x,y,z)+\epsilon_{yy}(x,y,z)+\epsilon_{zz}(x,y,z) \\ h_2(x,y,z) &= \gamma_{yz}(x,y,z) \\ h_3(x,y,z) &= y\gamma_{yz}(x,y,z) \\ h_4(x,y,z) &= z\gamma_{yz}(x,y,z) \\ h_5(x,y,z) &= \gamma_{zx}(x,y,z) \\ h_6(x,y,z) &= z\gamma_{zx}(x,y,z) \\ h_7(x,y,z) &= x\gamma_{zx}(x,y,z) \\ h_8(x,y,z) &= \gamma_{xy}(x,y,z) \\ h_9(x,y,z) &= x\gamma_{xy}(x,y,z) \\ h_{10}(x,y,z) &= y\gamma_{xy}(x,y,z) \end{aligned} \tag{27}$$

The computational effort for each 3-D FFT is of order $N_xN_yN_z(\log_2(N_x) + \log_2(N_y) + \log_2(N_z))$ operations, whereas that for assembling the elements of **M** from the resulting coefficients is of order $N_F^2 \sim 64M^2N^2O^2$ operations. The latter dominates over the former for problems involving relatively large numbers of Fourier coefficients in the reconstruction. In such cases, the computational effort becomes essentially independent of the resolution of the experimental strain fields, with a theoretical reduction in computational effort by a factor of $N_xN_yN_z$ by using the fast algorithm over the direct (i.e., element by element) method of assembling the matrix **M**.

The computation time for the other steps in the algorithm, i.e. evaluation of the terms in the vector **Y**; finding the solution of Eq. (12) by Gauss elimination; and reconstruction of the elastic stiffness distribution from the solution vector, is normally short compared to that for calculation of **M**. For example, the reconstruction of stiffness distribution from its Fourier coefficients can be handled very efficiently by performing a single 3-D inverse Fourier transform on a 3-D block of complex numbers, where the calculated $a_{m,n,o}$ and $b_{m,n,o}$ coefficients are the real and imaginary parts, respectively.

In the 'egg-box' stiffness distribution problem considered in Section 3.1 for example, the total time to set up matrix **M** involving nearly ten thousand degrees of freedom and a million elements of input strains using the fast algorithm on an Intel® Core™ i7 CPU 2.79 GHz computer with 8GB of memory was ~18s, compared to ~1.2×10^6s for the direct implementation of the same matrix. The time taken to invert Eqn. (12) was 167s. A time saving of 4-5 orders of magnitude is therefore clearly achievable in practice.

2.2. Adaptation of the 3-D F-VFM to unknown boundary conditions

As presented in Eq. (12) to (15) with the Fourier series parameterisation of the stiffness distribution in Eq. (8), the computation of the unknown coefficient vector **X** from the matrix Eq. (12) is in principle straightforward if the traction vector $\mathbf{T} = (T_x, T_y, T_z)$ necessary to establish the column vector **Y** is given. In reality however, these tractions might not be well specified, or even available at all. This section considers the case where knowledge of the traction vector **T** is not available over the boundary. It therefore requires a slight adaptation of the general F-VFM presented above. The adaptation can be done in (at least) three different ways, which we call the 'experimental traction', the 'windowed traction' and the 'Fourier-series traction' approaches. The former relies on the experimental strain field along

the boundary, which is converted to traction distributions via the recovered stiffness distribution. The second applies a window function to the virtual displacement fields so that the virtual work done by the tractions is identically equal to zero, regardless of the tractions. The third involves performing a Fourier series expansion of the traction distribution over the boundary, the coefficients for which are solved for at the same time as the unknown Fourier coefficients of the stiffness expansion. A comparison of the approaches can be found in [26]. The 'experimental traction' approach was found to be less robust in the presence of noise than the other two. In view of the relative simplicity of the 'windowed traction' approach over the 'Fourier-series traction' approach, the former was used to obtain all the results in this paper.

In the 'windowed traction' approach, continuity of the window function and its first derivative is required in order to ensure that the windowed virtual strains are well defined over the whole domain. A rectangular window function, for example, does not satisfy this requirement.

To simplify the mathematical derivation of the approach, we focus on a regular geometry such as the cuboid in Fig. 1. The virtual works of the tractions can then be broken down into six groups corresponding to the six faces of the cuboid:

$$\int_{S_f} \left(T_x u_x^* + T_y u_y^* + T_z u_z^*\right) dS_f = \sum_{i=1}^{6} \int_{S_f^{[i]}} \left(T_x^{[i]} u_x^* + T_y^{[i]} u_y^* + T_z^{[i]} u_z^*\right) dS_f^{[i]} \tag{28}$$

where $dS_f^{[i]}$ represents a surface element on face *i* and $T_x^{[i]}$, $T_y^{[i]}$, $T_z^{[i]}$ are the *x*, *y* and *z* components of the traction on the same face.

If we denote $W_x = W_x(x)$, $W_y = W_y(y)$ and $W_z = W_z(z)$ the functions chosen so as to zero the virtual displacements on faces 1 and 4, faces 2 and 5, and faces 3 and 6 respectively (refer to Fig. 1), $W(x, y, z) = W_x(x)W_y(y)W_z(z)$ is a potential combined window function that zeros the virtual works of the tractions over the boundary. The windowed virtual displacement fields $\hat{u}_x^*$, $\hat{u}_y^*$ and $\hat{u}_z^*$ are defined by multiplying the reference virtual displacements u_x^*, u_y^* and u_z^* by $W(x, y, z)$ so that $\hat{u}_x^* = W(x, y, z)u_x^*$, $\hat{u}_y^* = W(x, y, z)u_y^*$ and $\hat{u}_z^* = W(x, y, z)u_z^*$ are zero on the boundary. In what follows, the '^' symbol above a given variable indicates that it is windowed. Vector **Y** after applying this window function hence becomes zero as:

$$\widehat{\mathbf{Y}} = \begin{pmatrix} \sum_{i=1}^{6} \int_{S_f^{[i]}} \left(T_x^{[i]} \hat{u}_x^{*(1)} + T_y^{[i]} \hat{u}_y^{*(1)} + T_z^{[i]} \hat{u}_z^{*(1)} \right) dS_f^{[i]} \\ \vdots \\ \sum_{i=1}^{6} \int_{S_f^{[i]}} \left(T_x^{[i]} \hat{u}_x^{*(N_F)} + T_y^{[i]} \hat{u}_y^{*(N_F)} + T_z^{[i]} \hat{u}_z^{*(N_F)} \right) dS_f^{[i]} \end{pmatrix} = \mathbf{0} \tag{29}$$

The windowed matrix equation (12) with its right-hand-side vector $\widehat{\mathbf{Y}}$ being zero is thus of homogeneous form

$$\widehat{\mathbf{M}}\mathbf{X} = \mathbf{0} \tag{30}$$

with

$$\widehat{\mathbf{M}} = \begin{pmatrix} \int_V \hat{P}^{(1)} dV & \dots \int_V \hat{P}^{(1)} c_{m,n,o} dV \dots & \dots \int_V \hat{P}^{(1)} s_{m,n,o} dV \dots \\ \vdots & \vdots & \vdots \\ \int_V \hat{P}^{(N_F)} dV & \dots \int_V \hat{P}^{(N_F)} c_{m,n,o} dV \dots & \dots \int_V \hat{P}^{(N_F)} s_{m,n,o} dV \dots \end{pmatrix} \tag{31}$$

$$\begin{aligned} \hat{P} = \hat{P}(x,y,z) = & \left(\epsilon_{xx} + \frac{\nu}{1-\nu} (\epsilon_{yy} + \epsilon_{zz}) \right) \hat{\epsilon}_{xx}^* + \left(\epsilon_{yy} + \frac{\nu}{1-\nu} (\epsilon_{xx} + \epsilon_{zz}) \right) \hat{\epsilon}_{yy}^* \\ & + \left(\epsilon_{zz} + \frac{\nu}{1-\nu} (\epsilon_{xx} + \epsilon_{yy}) \right) \hat{\epsilon}_{zz}^* + \frac{1-2\nu}{2(1-\nu)} (\gamma_{yz} \hat{\gamma}_{yz}^* + \gamma_{zx} \hat{\gamma}_{zx}^* + \gamma_{xy} \hat{\gamma}_{xy}^*) \end{aligned} \tag{32}$$

and $\mathbf{X}$ the column vector of unknown Fourier stiffness coefficients defined in Eq. (14). The windowed virtual strain fields are obtained by differentiating the corresponding windowed virtual displacements $\hat{u}_x^*$, $\hat{u}_y^*$ and $\hat{u}_z^*$ as follows:

$$\begin{aligned} \hat{\epsilon}_{xx}^* &= \frac{\partial \hat{u}_x^*}{\partial x} = \frac{\partial (W u_x^*)}{\partial x} = W_{x,x} W_y W_z u_x^* + W \frac{\partial u_x^*}{\partial x} \\ \hat{\epsilon}_{yy}^* &= \frac{\partial \hat{u}_y^*}{\partial y} = \frac{\partial (W u_y^*)}{\partial y} = W_{y,y} W_x W_z u_y^* + W \frac{\partial u_y^*}{\partial y} \\ \hat{\epsilon}_{zz}^* &= \frac{\partial \hat{u}_z^*}{\partial z} = \frac{\partial (W u_z^*)}{\partial z} = W_{z,z} W_x W_y u_z^* + W \frac{\partial u_z^*}{\partial z} \end{aligned} \tag{33}$$

$$\hat{\gamma}_{yz}^{*} = \frac{\partial \hat{u}_y^*}{\partial z} + \frac{\partial \hat{u}_z^*}{\partial y} = \frac{\partial \left(W u_y^*\right)}{\partial z} + \frac{\partial (W u_z^*)}{\partial y}$$
$$= W_{z,z} W_x W_y u_y^* + W \frac{\partial u_y^*}{\partial z} + W_{y,y} W_x W_z u_z^* + W \frac{\partial u_z^*}{\partial y}$$

$$\hat{\gamma}_{zx}^{*} = \frac{\partial \hat{u}_z^*}{\partial x} + \frac{\partial \hat{u}_x^*}{\partial z} = \frac{\partial (W u_z^*)}{\partial x} + \frac{\partial (W u_x^*)}{\partial z}$$
$$= W_{x,x} W_y W_z u_z^* + W \frac{\partial u_z^*}{\partial x} + W_{z,z} W_x W_y u_x^* + W \frac{\partial u_x^*}{\partial z}$$

$$\hat{\gamma}_{xy}^{*} = \frac{\partial \hat{u}_x^*}{\partial y} + \frac{\partial \hat{u}_y^*}{\partial x} = \frac{\partial (W u_x^*)}{\partial y} + \frac{\partial \left(W u_y^*\right)}{\partial x}$$
$$= W_{y,y} W_x W_z u_x^* + W \frac{\partial u_x^*}{\partial y} + W_{x,x} W_y W_z u_y^* + W \frac{\partial u_y^*}{\partial x}$$

The reference virtual displacements u_x^*, u_y^*, u_z^* and their associated derivatives are specified in Table 1. The homogeneous matrix equation (30) has the trivial solution $\mathbf{X} = \mathbf{0}$, which is not useful here because we require a unique and non-zero stiffness distribution.

A normalisation strategy (see, e.g. [27]-chapter 3) can however be used in which the entire Fourier series stiffness expansion is divided by its dc term $a_{0,0,0}$, resulting in a unit dc term. With this approach, matrix $\widehat{\mathbf{M}}$ of size $N_F \times N_F$ can be split into a column vector $\widehat{\overline{\mathbf{N}}}$ of size $N_F \times 1$ and a sub-matrix $\widehat{\overline{\mathbf{M}}}$ of size $N_F \times (N_F - 1)$. The column vector $\widehat{\overline{\mathbf{N}}}$ is in fact the first column of matrix $\widehat{\mathbf{M}}$ which contains data corresponding to the unit dc term, and sub-matrix $\widehat{\overline{\mathbf{M}}}$ contains the rest of the data. $\widehat{\overline{\mathbf{N}}}$ is then brought to the right side of Eq. (30) resulting in the non-homogeneous and over-determined system of equations below:

$$\widehat{\overline{\mathbf{M}}} \overline{\mathbf{X}} = \widehat{\overline{\mathbf{N}}} \tag{34}$$

This equation can be solved for its normalised coefficient vector $\overline{\mathbf{X}}$ in a least-squares sense using e.g. the Moore-Penrose inversion algorithm[2].

The formulae for $\widehat{\overline{\mathbf{M}}}$, $\widehat{\overline{\mathbf{N}}}$ and $\overline{\mathbf{X}}$ are

[2] The Moore-Penrose inversion is implemented in MATLAB using command `pinv`.

$$\widehat{\overline{\mathbf{M}}} = \begin{pmatrix} \dots \int_V \hat{P}^{(1)} c_{m,n,o} dV \dots & \dots \int_S \hat{P}^{(1)} s_{m,n,o} dV \dots \\ \vdots & \vdots \\ \dots \int_V \hat{P}^{(N_F)} c_{m,n,o} dV \dots & \dots \int_V \hat{P}^{(N_F)} s_{m,n,o} dV \dots \end{pmatrix} \tag{35}$$

$$\widehat{\overline{\mathbf{N}}} = -\begin{pmatrix} \int_V \hat{P}^{(1)} dV \\ \vdots \\ \int_V \hat{P}^{(N_F)} dV \end{pmatrix} \tag{36}$$

$$\overline{\mathbf{X}} = \frac{1}{a_{0,0,0}} (\dots a_{m,n,o} \dots \quad \dots b_{m,n,o} \dots)' \tag{37}$$

The stiffness distribution reconstructed from the Fourier coefficients in vector $\overline{\mathbf{X}}$ is thus a scaled version of the real distribution by a factor of the dc term $a_{0,0,0}$ due to the normalisation needed to obtain a unique solution to the homogeneous equation. The stiffness identification by the F-VFM in the case of unknown boundary conditions can therefore only be achievable to within an unknown scale factor.

2.3. Adaptation to incompressible materials

Although the F-VFM mentioned earlier can theoretically be applied to nearly all types of isotropic elastic materials, the use of Eq. (5) might not provide accurate results if the material is nearly incompressible as some components of the stiffness matrix in Eq. (3) tend to infinity as ν tends to 0.5. The equation therefore needs to be adapted to this particular type of material.

According to [28] the constitutive relation of incompressible materials can be written in matrix form to reveal the contribution of the shear modulus term as:

$$\boldsymbol{\sigma} = -\mathbf{p} + 2G\boldsymbol{\epsilon} \tag{38}$$

in which $\boldsymbol{\sigma} = \{\sigma_{xx}, \sigma_{yy}, \sigma_{zz}, \tau_{yz}, \tau_{zx}, \tau_{xy}\}'$ and $\boldsymbol{\epsilon} = \{\epsilon_{xx}, \epsilon_{yy}, \epsilon_{zz}, \gamma_{yz}, \gamma_{zx}, \gamma_{xy}\}'$ are respectively column vectors containing components of the stress and strain tensors; $\mathbf{p} =$

$\{p, p, p, 0,0,0\}'$ is the vector of the hydrostatic pressure p; G the shear modulus distribution of the material (which in some textbooks is denoted by μ). The substitution of Eq. (38) into Eq. (1) yields the essential equation of the VFM written for incompressible materials:

$$-\int_V \mathbf{p}\boldsymbol{\epsilon}^* \mathrm{d}V + 2\int_V G\boldsymbol{\epsilon}\boldsymbol{\epsilon}^* \mathrm{d}V = \int_{S_f} \mathbf{T}\cdot\mathbf{u}^* \mathrm{d}S_f \tag{39}$$

The contribution of the hydrostatic pressure $\mathbf{p}$ in Eq. (39) is not easily measured and cannot be neglected in general. However, with a special choice of the virtual fields, and under the assumption that pressure gradients can be neglected, one can remove the involvement of the hydrostatic pressure term in the Eq. (39)[3]. This approximation, which was proposed in [16] when analysing the same dataset using the FE-based VFM, can be seen by considering the term which contains the hydrostatic pressure $\int_V \mathbf{p}\boldsymbol{\epsilon}^* dV$. By integrating this term by parts one gets

$$\int_V \mathbf{p}\boldsymbol{\epsilon}^* dV = \int_V \mathbf{p}(\nabla\mathbf{u}^*) dV = \mathbf{p}\int_{S_f} \mathbf{u}^* dS_f - \int_V \mathbf{u}^*(\nabla\mathbf{p}) dV \tag{40}$$

If the virtual displacement field $\mathbf{u}^*$ is chosen to be zero over the boundary of the volume V (which is indeed possible and is presented later in this paper through the application of a potential window function to the virtual displacements), the integrals $\mathbf{p}\int_{S_f} \mathbf{u}^* dS_f$ and $\int_V \mathbf{u}^*(\nabla\mathbf{p}) dV$ involving gradient of the hydrostatic pressure term will become zeros, allowing the integral $\int_V \mathbf{p}\boldsymbol{\epsilon}^* dV$ to be neglected. As a result Eq. (39) can be reformulated in a more simple form as follows:

$$\int_V 2G\boldsymbol{\epsilon}\boldsymbol{\epsilon}^* \mathrm{d}V = \int_{S_f} \mathbf{T}\cdot\mathbf{u}^* \mathrm{d}S_f \tag{41}$$

which only has G as the unknown variable. The shear modulus distribution G relates to the elastic parameters E and ν of an incompressible material by

$$G = \frac{E}{2(1+\nu)} = \frac{E}{3} \tag{42}$$

[3] The gradient of pressure $\mathbf{p}$ is null if p is assumed to be uniform. In the case where p is not uniform, zeroing $\mathbf{u}^*$ at the boundary will not cancel the contribution of $\mathbf{p}$ to the virtual work, which otherwise requires the choice of $\mathbf{u}^*$ satisfying div($\mathbf{u}^*$) = 0 throughout the volume to fully cancel $\mathbf{p}$. One example of virtual fields that satisfy div($\mathbf{u}^*$) = 0 is given in [29]; unfortunately, however, the cosine/sine functions used in the F-VFM method do not satisfy this constraint.

Eq. (41) now looks identical to Eq. (2) except for the notation of G being used instead of Q. The F-VFM re-derived for incompressible materials can therefore be replicated from that derived in the general case, as in the previous section, starting with the unknown shear modulus G being parameterised by a Fourier series.

3. Examples with numerical and experimental data

In this section we show proof-of-principle results of the 3-D F-VFM presented above. Numerical input strain data were achieved from a forward analysis using a commercial finite element package. Sensitivity analyses demonstrate the impact of noise on the performance of the F-VFM using numerical input. Application to real experimental data shows a successful implementation of the technique derived for incompressible materials, in the case of unknown boundary conditions.

3.1. Example with numerical data and known boundary conditions

A cube of size $L_x \times L_y \times L_z = 10 \times 10 \times 10$ mm^3 was subject to uniform tri-axial traction distributions of magnitude $\sigma_0 = 1$ MPa perpendicular to all six faces of the cube and pointing outwards. The linearity of the model and F-VFM equations means that equivalent results would also have been obtained with uniform compression rather than tension. The cube was defined to consist of a linear elastic isotropic material of Poisson's ratio $\nu = 0.3$ and with an elastic modulus distribution of an 'egg-box' pattern defined by

$$E^{\text{ref}} = 20 + \cos 2\pi\left(\frac{2x}{L_x} + \frac{y}{L_y} + \frac{2z}{L_z}\right) + \sin 2\pi\left(\frac{x}{L_x} + \frac{2y}{L_y} + \frac{2z}{L_z}\right) \tag{43}$$

where the units of E^{ref} are MPa. The origin of the coordinate system is located at the centroid of the cube. The corresponding 3-D stiffness distribution follows from Eq. (4) as:

$$Q_{xx}^{\text{ref}} = 26.92 + 1.35\cos 2\pi\left(\frac{2x}{L_x} + \frac{y}{L_y} + \frac{2z}{L_z}\right) + 1.35\sin 2\pi\left(\frac{x}{L_x} + \frac{2y}{L_y} + \frac{2z}{L_z}\right) \tag{44}$$

and its normalised version $\bar{Q}_{xx}^{\text{ref}}$ is deduced by scaling down the reference stiffness Q_{xx}^{ref} by its dc term, i.e.

$$\bar{Q}_{xx}^{\text{ref}} = \frac{Q_{xx}^{\text{ref}}}{26.92} = 1 + 0.05\cos 2\pi\left(\frac{2x}{L_x} + \frac{y}{L_y} + \frac{2z}{L_z}\right) + 0.05\sin 2\pi\left(\frac{x}{L_x} + \frac{2y}{L_y} + \frac{2z}{L_z}\right) \tag{45}$$

Q_{xx}^{ref} has units of MPa, and $\bar{Q}_{xx}^{\mathrm{ref}}$ is non-dimensional.

The geometry was meshed in Mentat2010 (the pre/post-processing module of the commercial finite element package MscMarc™2010) using 100×100×100 eight-node hexahedral volume elements (HEX8) with full integration. The model was then analysed in Marc2010 and six strain components ϵ_{xx}, ϵ_{yy}, ϵ_{zz}, γ_{yz}, γ_{zx} and γ_{xy} were returned.

The fact that the traction distributions are known in this case means that vector **Y** of Eq. (15) can be determined. Due to the symmetry of the cubic model, the integral of 6 traction components can be reduced to a summation of 3 identical sub-integrals of the form $\int_{S_f^{[i]}} T_i u_i^* dS_f^{[i]}$ in which $i = x, y$ or z and $S_f^{[i]}$ is the surface perpendicular to the ith-direction over which the integral is calculated. The product between the traction T_i and the infinitesimal surface element $dS_f^{[i]}$ can be approximated as a small concentrated force applied to the surface of each element. This product can be simply calculated as $T_i dS_f^{[i]} = T_i \frac{l_i}{N_\epsilon^{(i)}} \frac{l_j}{N_\epsilon^{(j)}} = 1\left[\frac{N}{mm^2}\right] \times \frac{10}{100}[mm] \times \frac{10}{100}[mm] = 0.01[N]$; with $i, j = x, y, z$ and $N_\epsilon^{(\alpha)}$ the number of elements along direction α. This value is constant on every element. If $N_\epsilon^{(\alpha)}$ is large enough, the initial sub-integral can be approximated by the summation of corresponding virtual displacements times the elementary force $T_i dS_f^{[i]}$.

The six strain components ϵ_{xx}, ϵ_{yy}, ϵ_{zz}, ϵ_{yz}, ϵ_{zx} and ϵ_{xy} obtained from the forward finite element analysis of the cube were used as input data to the 3-D F-VFM script. The unknown Fourier series coefficients of the stiffness distribution were then calculated from the resolution equation (12), with the virtual fields summarised in Table 1. In this calculation, the number of cosine/sine terms of the stiffness Fourier series (9) took the value $M = N = O = 15$, which theoretically results in a total of $N_F = 30751$ unknowns using Eq. (16). However this number can be reduced to 8191 unknowns by assuming that the stiffness Fourier series only consists of non-negative frequency terms due to the fact that the reference egg-box pattern only contains positive frequencies as presented in Eq. (44). This assumption is only made in this particular problem for the purpose of reducing the number of degrees of freedom. The chosen values for M, N and O are significantly higher than the value 2 that would be required to fully represent the stiffness distribution in Eq. (44) and (45), in order to provide a more realistic simulation of the performance of the algorithm on real data in the presence of noise.

The stiffness distribution of the 3-D ‘egg-box’ pattern reconstructed by the F-VFM is presented in Fig. 2(c). Even though they are not always clearly seen, ripples at the highest spatial frequency of the Fourier series stiffness expansion exist in the reconstructed result, in a similar way to those observed in the 2-D F-VFM [18, 19, 30]. Also as in the 2-D case, these can be filtered out by convolving the recovered stiffness distribution with an appropriate kernel. In this case a cuboid kernel was chosen, where the length of each side is equal to the pitch of the ripples along the corresponding axis. Further details of the filtering can be found in [26]. Ripple filtering does however result in a thin shell of low magnitude over the faces of the cuboid stiffness map. This is due to the fact that any point within a distance of half the pitch from the outer faces is influenced by the stiffness values outside the volume of interest, which are unknown and here assumed to be zero. In Fig. 2(c) to (f), this thin shell of low magnitude has been removed from the reconstructed stiffness distributions for clarity. The error distribution of the recovered stiffness in Fig. 2(d) shows a root mean square error value of ~0.1% whereas that of the unfiltered stiffness is ~0.3%.

Sensitivity of the technique to different noise levels was also investigated in the context of the 3-D ‘egg-box’ pattern. Gaussian noise patterns of 10 different standard deviations σ ranging from 10^{-3} mm to 10^{-2} mm were introduced to the original displacements. The differentiation for strains from noisy displacements was carried out with 2 different kernel sizes 3×3×3 and 7×7×7 pixels, respectively. At each noise level, 50 computations corresponding to 50 random noise patterns were implemented, resulting in a total of 500 stiffness reconstructions. The mean value of every set of 50 stiffness patterns reconstructed by the F-VFM at discrete noise levels, and its standard deviation, are plotted in Fig. 3. An example of a recovered ‘egg-box’ stiffness pattern at medium noise level $\sigma = 5\times10^{-3}$ mm is shown in Fig. 2(e) with a root mean square error of the stiffness reconstruction of ~0.7%. The corresponding error map is shown in Fig. 2(f).

3.2. Example with numerical data and unknown boundary conditions

This section uses the numerical strain data of the artificial ‘egg-box’ model under tri-axial loading conditions from the previous section. The information about the traction boundary conditions is, however, now assumed unknown. Distributions of stiffness and tractions are then reconstructed by the ‘windowed traction’ approach of the F-VFM described in section

2.2. Stiffness reconstruction was carried out with the choice of $M = N = O = 15$, resulting in a total of 8190 unknown coefficients.

A cosine window function of the form $W(x, y, z) = W_x(x)W_y(y)W_z(z)$ was used in this example where

$$\begin{cases} W_x = \cos\dfrac{\pi x}{L_x}; W_{x,x} = -\dfrac{\pi}{L_x}\sin\dfrac{\pi x}{L_x}; W_{x,y} = 0;\ W_{x,z} = 0 \\ W_y = \cos\dfrac{\pi y}{L_y}; W_{y,y} = -\dfrac{\pi}{L_y}\sin\dfrac{\pi y}{L_y}; W_{y,z} = 0; W_{y,x} = 0 \\ W_z = \cos\dfrac{\pi z}{L_z}; W_{z,z} = -\dfrac{\pi}{L_z}\sin\dfrac{\pi z}{L_z}; W_{z,x} = 0; W_{z,y} = 0 \end{cases} \tag{46}$$

The 'egg-box' stiffness distribution reconstructed by the 'windowed traction' approach is presented in Fig. 4. The root mean square error of the stiffness reconstruction increases from ~0.2% in the noise-free case (Fig. 4(b)) to ~3% in the presence of noise (Fig. 4(d)). The root mean square errors show the effect of high frequency terms being magnified by the noise, which becomes more severe than the case shown in Fig. 2.

Distributions of unknown tractions can also be deduced from the corresponding reconstructed stiffness and measured strains using the formulae:

$$\begin{aligned} T_x &= \left(\epsilon_{xx} + \frac{\nu}{1-\nu}\left(\epsilon_{yy} + \epsilon_{zz}\right)\right) Q_{xx} \quad \text{(faces 1,4)} \\ T_y &= \left(\epsilon_{yy} + \frac{\nu}{1-\nu}\left(\epsilon_{xx} + \epsilon_{zz}\right)\right) Q_{xx} \quad \text{(faces 2,5)} \\ T_z &= \left(\epsilon_{zz} + \frac{\nu}{1-\nu}\left(\epsilon_{xx} + \epsilon_{yy}\right)\right) Q_{xx} \quad \text{(faces 3,6)} \end{aligned} \tag{47}$$

In Fig. 5 the results of traction distribution reconstructions, with and without noise in the input strain fields, can be seen in comparison with the (normalised) amplitude of the reference traction of ~0.037 in a similar way to that described in section 3.1. It is worth noting that the reconstructed stiffness used to recover the tractions in Fig. 5 was not smoothed/ filtered due to the fact that data filtering generates a thin layer of low magnitude stiffness near the surfaces, which then introduces significantly more errors to the recovered tractions. The graph in Fig. 6 shows the sensitivity of the stiffness recovered by the 'windowed traction' approach to different signal-to-noise ratios. Both kernel sizes result in a similar mean error, but the smaller kernel (size 3×3×3) has more variability in the calculated stiffness than does the larger one as the noise level increases.

3.3. Example with experimental data of incompressible materials

In this section, the 3-D F-VFM is applied to the experimental MRI data of a two-phase test sample presented in [4]. The sample is a tissue-mimicking phantom of cuboidal shape of size 80×64×154 mm^3, having a spherical inclusion of 25mm diameter at the centre. Semicosil 921 silicone gel with different mixing ratios was used to create the harder inclusion and the softer background material. The phantom was placed within the magnetic field of a MRI instrument for measuring its full-field displacements whilst a vertical displacement of ~2.4mm was applied to the phantom in the *y*-direction. Measurements on a force-deformation system [31] demonstrated that the inclusion is four times stiffer than the surrounding material, and that both phases were deformed within their elastic limits. Fig. 7 shows an eighth of the sample with uniform displacement boundary conditions applied to its top surface along the vertical axis. Details of how the signals were acquired and manipulated were presented in [16]. Raw data obtained from the MRI system are very noisy near the outer faces of the phantom and needed to be removed. Therefore, only data around the inclusion, covering a volume of 46.41×46.72×42.19 mm^3 (the volume highlighted in grey in Fig. 7) with 115×141×36 voxels inside it, were used. The origin of the measuring coordinate system is set to be at the centroid of the volume of interest. Since the useful measurement data do not occupy the entire volume of the phantom, traction distributions over the surfaces of the grey volume are not available. The 'windowed traction' approach was therefore used for the identification of the shear modulus distribution.

The limits of the shear modulus Fourier series summation were chosen to be $M = N = O = 9$ (covering both positive and negative frequencies), resulting in a total of 7219 unknown Fourier coefficients. The reason for *M*, *N* and *O* taking the specific value 9 is explained in the last paragraph of this section. The window function $W = (x - \frac{L_x}{2})(x + \frac{L_x}{2})(y - \frac{L_y}{2})(y + \frac{L_y}{2})(z - \frac{L_z}{2})(z + \frac{L_z}{2})$ which is identical to the one used in [16], was used for the identification. Application of the fast algorithm to the 'windowed traction' approach returned the shear modulus distribution in less than 3 minutes. The reconstructed modulus distribution is presented in Fig. 8(a) in the form of 36 cross-sections normal to the *z*-direction and compared with results from a finite-element based VFM in Fig. 8(b) and from the magnitude of the MRI signal in Fig. 8(c). No filtering of the modulus distribution was employed in this case.

In order to determine the modulus ratio between the inclusion and the more compliant background, the boundary between these regions must be determined. An estimator which bounds an ellipsoid around the region of higher modulus was used, similarly to the procedure in [16]. The ellipsoid is defined by 6 parameters: x_0, y_0, z_0 for the coordinates of the ellipsoid's centre, and r_x, r_y, r_z the half-lengths of the ellipsoid along its principal axes. The standard ellipsoid centred at (x_0, y_0, z_0) and aligned with the coordinate axes has the form:

$$\frac{(x-x_0)^2}{r_x^2}+\frac{(y-y_0)^2}{r_y^2}+\frac{(z-z_0)^2}{r_z^2}=1 \tag{48}$$

The 6 parameters which defined a unique ellipsoid were estimated through a simple `fminsearch` optimisation in MATLAB. The voxels whose centroids are inside this ellipsoid are considered as part of the inclusion, the rest belonging to the background material. An ellipsoid was used here instead of a sphere because the voxels do not have equal spacing along the three axes. Average modulus values are 2.64 for the higher modulus region (i.e. the inclusion) and 0.62 for the lower modulus region (i.e. background), resulting in a modulus ratio of 4.26 between the two phases. This value is not very different from the reference ratio of 4 reported in [4] using the measurement-based technique in [30], and 4.31 using a finite-element-based virtual fields method [16]. Normalised modulus values for each phase of the phantom and their ratios are summarised and compared in Table 2.

Several points regarding this result in relation to the finite-element-based method in [16] are worth making. Firstly, the finite-element-based VFM in [16] assumed that moduli of the voxels on the periphery took the values of 1. This assumption is, however, only appropriate if *a priori* knowledge about the phantom is given. The current F-VFM does not make any assumption about the modulus distribution in advance. Secondly, the authors in [16] only used strain field components along the y-direction (the loading direction) in the identification with the argument that these fields are more sensitive to the modulus variations than the others. The modulus reconstruction with the F-VFM, on the other hand, accounted for deformations in all directions. Thirdly, in terms of the numbers of degrees of freedom (dofs), the choice of $N = 9$ cosine/sine Fourier terms results in a total of ~10,000 unknowns whereas [16] generated ~120,000 unknowns, or ~12 times more dofs than those in the F-VFM. In principle, the number of dofs of the F-VFM can be further increased. However, the fast F-VFM algorithm with fast Fourier transforms was limited by the size of the experimental dataset. Indeed, the number of 36 voxels in z-direction of the strain data only allows possible

limits of the indices n and o in Eq. (9) of –9 to 9 so that the indices of the terms defined in Eq. (23) do not go beyond the range –18 to 18. This limitation can in principle be avoided by interpolation of the input strain fields, e.g. by Fourier transforming them, zero padding [32] and then inverse Fourier transforming.

4. Conclusions

The paper presents a development of the virtual fields method to reconstruct 3-D modulus distributions from measured full-field data. Like the previously-published VFM algorithms, modulus distributions are reconstructed after a single computation step without any iteration. By using a 3-D Fourier series expansion of the unknown modulus distribution, and cosine/sine waves for the virtual fields, an efficient numerical algorithm based on the fast Fourier Transform allows volume identification problems with ~10^4 degrees of freedom to be solved in just a few minutes. The technique can be readily adapted to the case of unknown boundary conditions, although it then only provides modulus distributions normalised with respect to the average modulus value. It has been validated with numerical data from a 3-D 'egg-box' stiffness pattern, for both the known and unknown boundary condition cases. Application of the technique to measured data of incompressible materials is possible, but requires a slightly different interpretation of the fundamental equation of the F-VFM. In the case studied, modulus results returned by the F-VFM are consistent with the values provided by other experimental and numerical techniques.

Table 1: Virtual displacement field components u_x^*, u_y^* and u_z^* and their derivatives used in the 3-D F-VFM.

Sub-matrix	p	u_x^*	$\frac{\partial u_x^*}{\partial x}$	$\frac{\partial u_x^*}{\partial y}$	$\frac{\partial u_x^*}{\partial z}$
A, B	0	$xc_{0,q,r}$	$c_{0,q,r}$	$-\frac{2\pi q}{L_y} xs_{0,q,r}$	$-\frac{2\pi r}{L_z} zs_{0,q,r}$
	> 0	$\frac{L_x}{2\pi p} s_{p,q,r}$	$c_{p,q,r}$	$\frac{L_x}{L_y}\frac{q}{p} c_{p,q,r}$	$\frac{L_x}{L_z}\frac{r}{p} c_{p,q,r}$
C, D	0	$xs_{0,q,r}$	$s_{0,q,r}$	$\frac{2\pi q}{L_y} xc_{0,q,r}$	$\frac{2\pi r}{L_z} zc_{0,q,r}$
	> 0	$-\frac{L_x}{2\pi p} c_{p,q,r}$	$s_{p,q,r}$	$\frac{L_x}{L_y}\frac{q}{p} s_{p,q,r}$	$\frac{L_x}{L_z}\frac{r}{p} s_{p,q,r}$
	q	u_y^*	$\frac{\partial u_y^*}{\partial x}$	$\frac{\partial u_y^*}{\partial y}$	$\frac{\partial u_y^*}{\partial z}$
A, B	0	$yc_{p,0,r}$	$-\frac{2\pi p}{L_x} ys_{p,0,r}$	$c_{p,0,r}$	$-\frac{2\pi r}{L_z} ys_{p,0,r}$
	> 0	$\frac{L_y}{2\pi q} s_{p,q,r}$	$\frac{L_y}{L_x}\frac{p}{q} c_{p,q,r}$	$c_{p,q,r}$	$\frac{L_y}{L_z}\frac{r}{q} c_{p,q,r}$
C, D	0	$ys_{p,0,r}$	$\frac{2\pi p}{L_x} yc_{p,0,r}$	$s_{p,0,r}$	$\frac{2\pi r}{L_z} yc_{p,0,r}$
	> 0	$-\frac{L_y}{2\pi q} c_{p,q,r}$	$\frac{L_y}{L_x}\frac{p}{q} s_{p,q,r}$	$s_{p,q,r}$	$\frac{L_y}{L_z}\frac{r}{q} s_{p,q,r}$
	r	u_z^*	$\frac{\partial u_z^*}{\partial x}$	$\frac{\partial u_z^*}{\partial y}$	$\frac{\partial u_z^*}{\partial z}$
A, B	0	$zc_{p,q,0}$	$-\frac{2\pi p}{L_x} zs_{p,q,0}$	$-\frac{2\pi q}{L_y} zs_{p,q,0}$	$c_{p,q,0}$
	> 0	$\frac{L_z}{2\pi r} s_{p,q,r}$	$\frac{L_z}{L_x}\frac{p}{r} c_{p,q,r}$	$\frac{L_z}{L_y}\frac{q}{r} c_{p,q,r}$	$c_{p,q,r}$
C, D	0	$zs_{p,q,0}$	$\frac{2\pi p}{L_x} zc_{p,q,0}$	$\frac{2\pi q}{L_y} zc_{p,q,0}$	$s_{p,q,0}$
	> 0	$-\frac{L_z}{2\pi r} c_{p,q,r}$	$\frac{L_z}{L_x}\frac{p}{r} s_{p,q,r}$	$\frac{L_z}{L_y}\frac{q}{r} s_{p,q,r}$	$s_{p,q,r}$

Table 2: Comparison of (average) shear moduli and their ratios identified by different methods.

Methods	Average values of non-dimensional modulus		Modulus ratio
	Background	Inclusion	
Measurement-based method [4, 31]	–	–	4.0
Finite-element-based VFM [16]	0.69	2.98	4.31
Fourier-series-based VFM	0.62	2.64	4.26

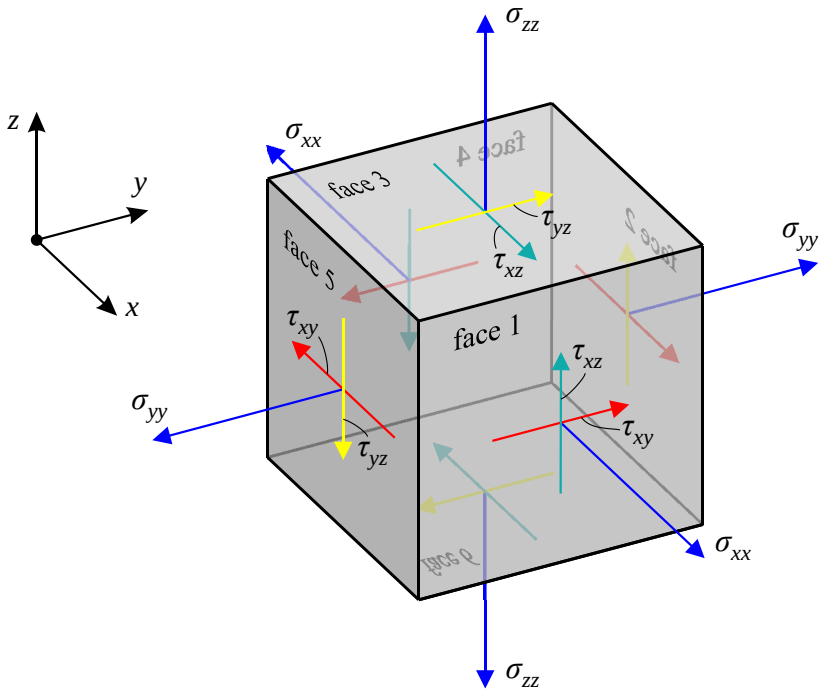

Fig. 1. Diagram of a cuboidal volume subject to normal and shear stresses (or tractions) over its faces.

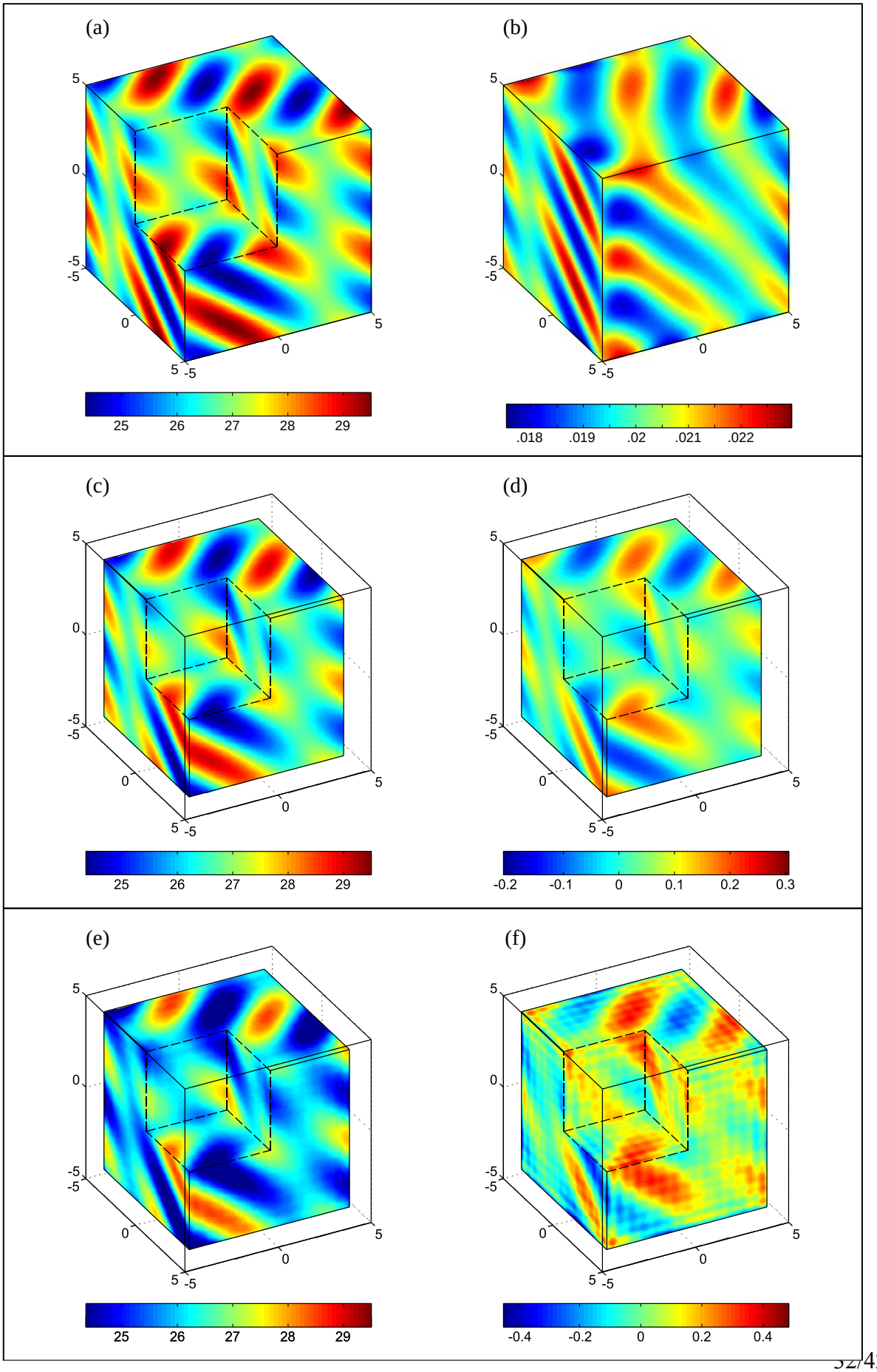
(a)
(b)
(c)
(d)
(e)
(f)
5
0
-5
25 26 27 28 29
.018 .019 .02 .021 .022
-0.2 -0.1 0 0.1 0.2 0.3
-0.4 -0.2 0 0.2 0.4

Fig. 2. Reconstruction of a 3-D ‘egg-box’ stiffness distribution, using highest normalised spatial frequencies $M = N = O = 15$ and known boundary conditions. (a) the reference ‘egg-box’ stiffness distribution, and (b) the corresponding strain distribution ϵ_{yy} from numerical analysis. (c) and (d) are respectively the reconstructed ‘egg-box’ stiffness using the 3-D F-VFM and its corresponding stiffness error (or the difference between (c) and the reference distribution (a)) in the noise-free case. (e) and (f) are respectively the same as (c) and (d) computed when Gaussian noise of standard deviation $\sigma = 5\times10^{-3}$ mm was introduced to the input displacement fields. In figures (c) to (f), a thin shell of low magnitude data around the cube due to the filtering technique was removed, and an eighth of the cube is cut out to allow information inside the cube to be visualised. The coordinate system is the same as in Fig. 1.

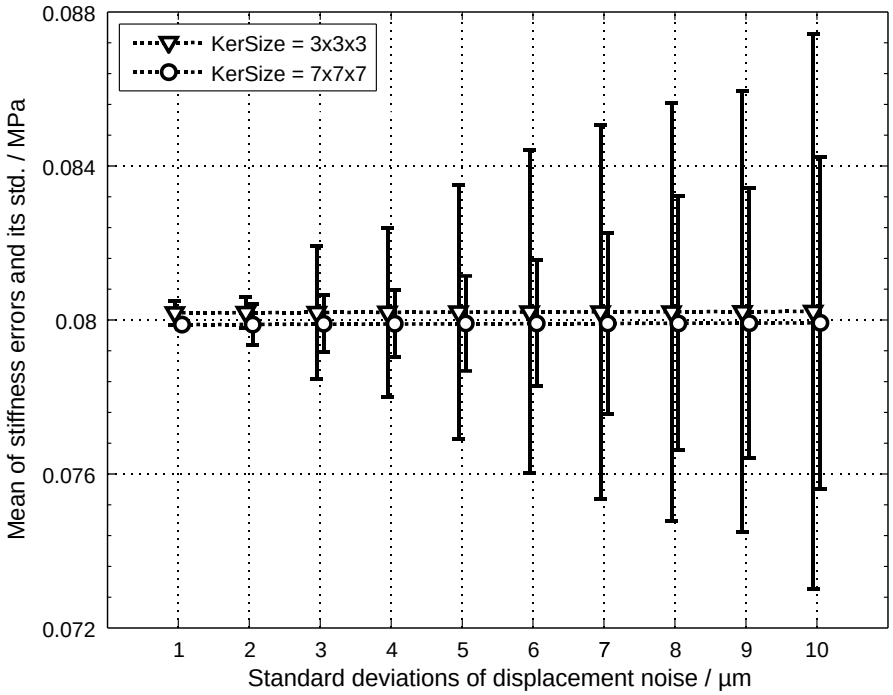

Fig. 3. Sensitivity of the 3-D F-VFM to a variety of noise levels in the identification of a 3-D 'egg-box' stiffness pattern, with known boundary tractions and $N = 15$. At each noise level, 50 computations corresponding to 50 random noise patterns from noisy displacements were implemented. The differentiation for strains from noisy displacements was carried out with two different kernel sizes: 3×3×3 and 7×7×7 pixels. The stiffness errors (markers) and the standard deviations in the mean of errors (error bars) were computed from the difference of the recovered stiffness after data smoothing/filtering with respect to the reference.

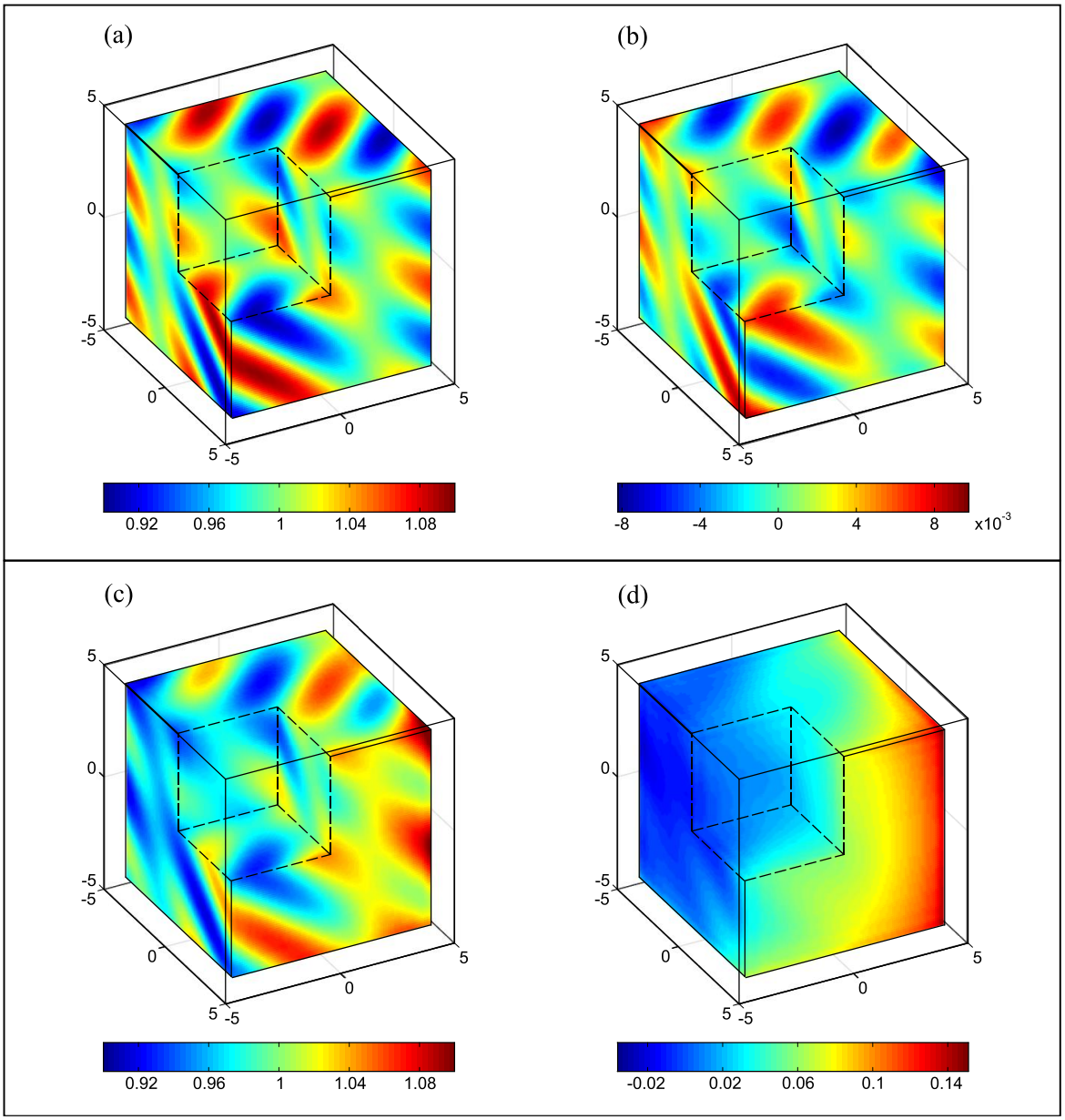

Fig. 4. Reconstruction of a normalised 3-D ‘egg-box’ stiffness pattern under unknown loading conditions using the ‘windowed traction’ technique at highest spatial frequencies $M = N = O = 15$. (a) and (b) are respectively the reconstructed ‘egg-box’ stiffness and its corresponding stiffness error (i.e., the difference between (a) and the normalised reference distribution) in the noise-free case. (c) and (d) are respectively the same as (a) and (b) computed when Gaussian noise of standard deviation $\sigma = 5\times10^{-3}$ mm was introduced to the input displacement fields. The coordinate system is the same as in Fig. 1.

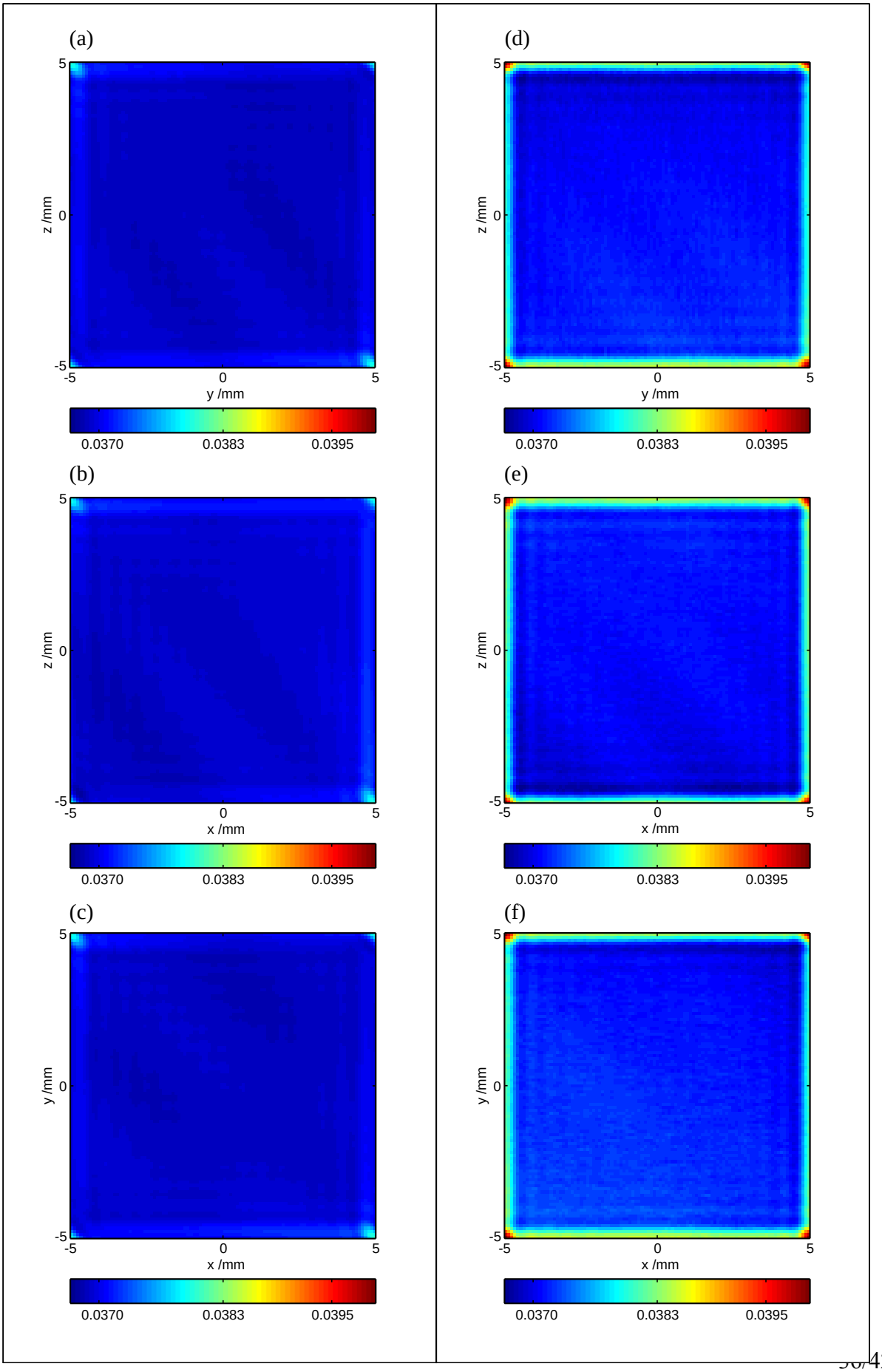
(a)
5
0
-5
z /mm
-5
0
5
y /mm
0.0370
0.0383
0.0395
(d)
5
0
-5
z /mm
-5
0
5
y /mm
0.0370
0.0383
0.0395
(b)
5
0
-5
z /mm
-5
0
5
x /mm
0.0370
0.0383
0.0395
(e)
5
0
-5
z /mm
-5
0
5
x /mm
0.0370
0.0383
0.0395
(c)
5
0
-5
y /mm
-5
0
5
x /mm
0.0370
0.0383
0.0395
(f)
5
0
-5
y /mm
-5
0
5
x /mm
0.0370
0.0383
0.0395

Fig. 5. Recovery of unknown non-dimensional traction distributions T_x, T_y and T_z (top down order) over the faces of a 3-D cube of an 'egg-box' stiffness pattern using the 'windowed traction' approach. Tractions are computed from their corresponding unfiltered stiffness maps, and the input strain fields. (a),(b),(c) are the noise-free case whilst (d),(e),(f) are for the medium noise case (standard deviation of 5×10^{-3} mm in the input displacement fields). The corresponding non-dimensional reference tractions take the value ~0.037.

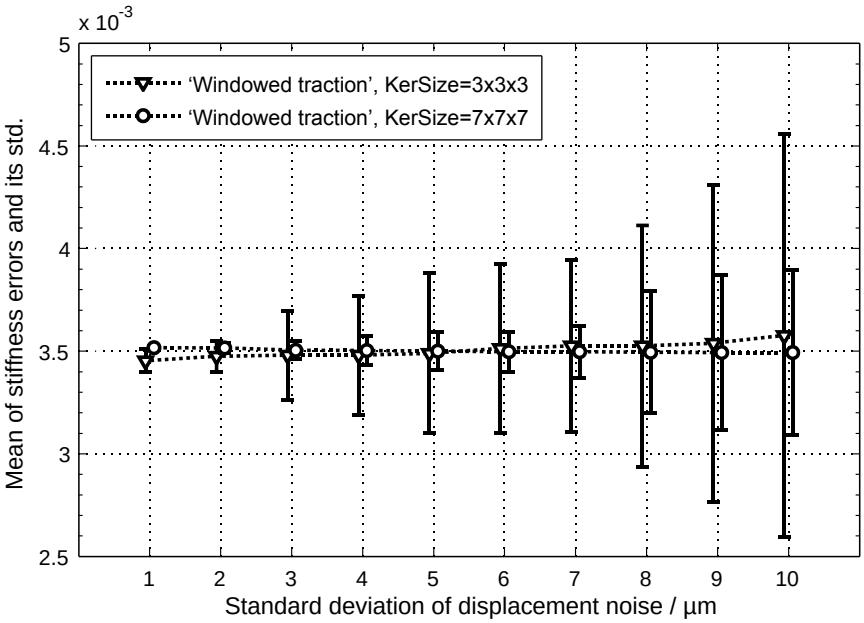

Fig. 6. Sensitivity of the F-VFM-adapted 'windowed traction' technique to a variety of noise levels in the identification of a (normalised) 3-D 'egg-box' stiffness pattern, with $N = 15$. At each noise level, 50 computations corresponding to 50 random noise patterns from noisy displacements were implemented. The differentiation for strains from noisy displacements was carried out with two different kernel sizes 3×3×3 and 7×7×7 pixels. The normalised stiffness errors (markers) and the standard deviations in the mean of errors (error bars) were computed from the difference of the recovered stiffness after data smoothing/filtering with respect to the reference. Stiffness values on vertical axis are normalised.

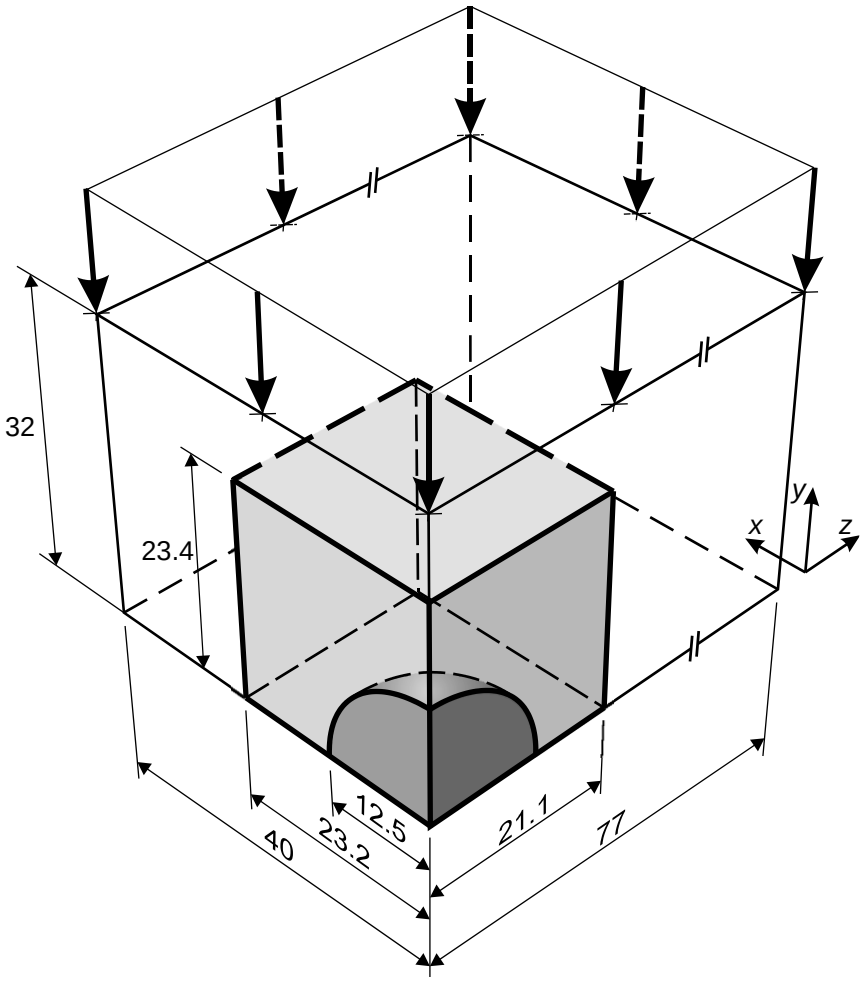

Fig. 7. Schematic of one eighth of the tested phantom under distributed compressive loads with the volume of interest being highlighted.

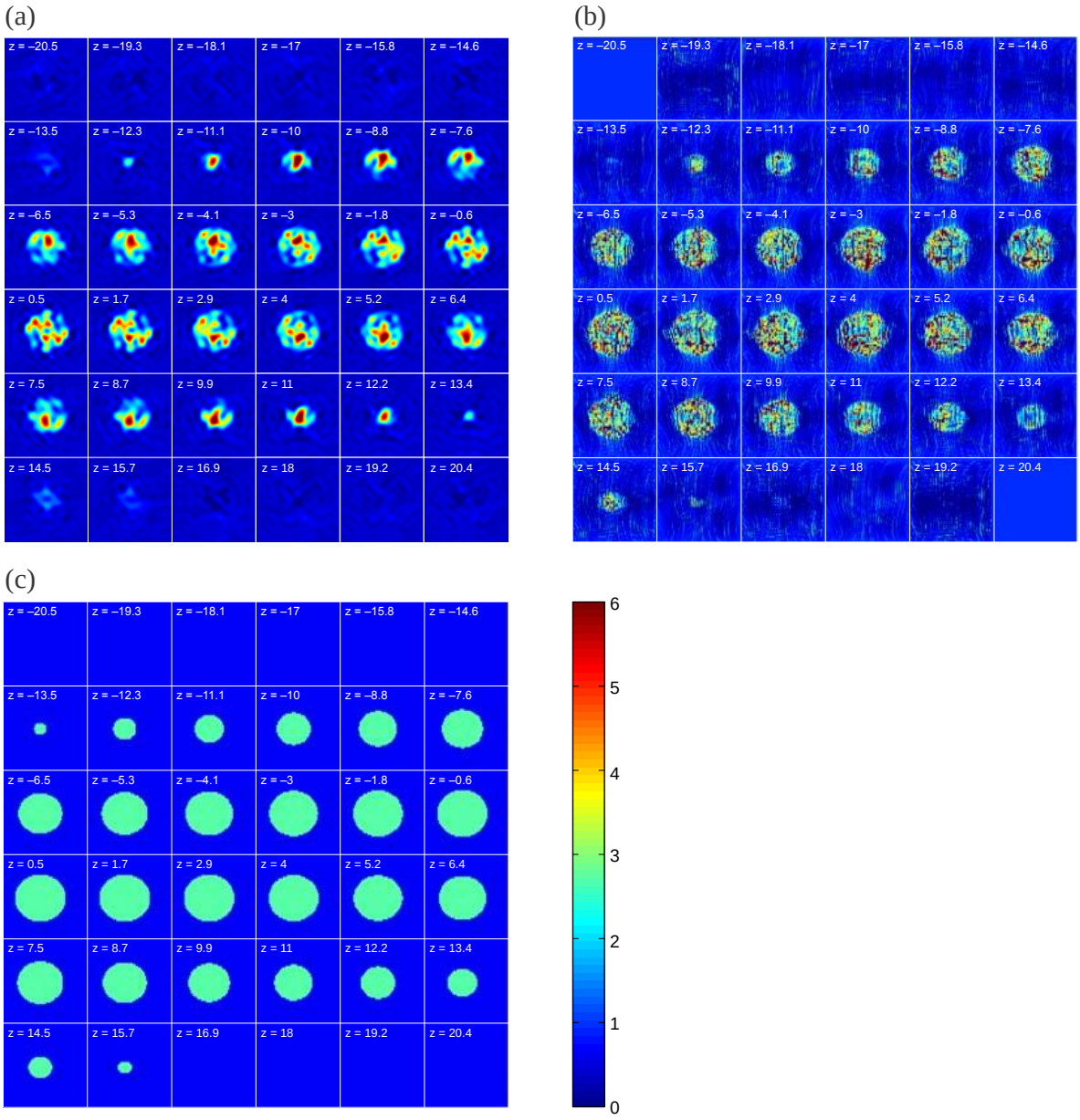

Fig. 8. Reconstruction of shear modulus distribution of a two-phase phantom from its MRI data by (a) the F-VFM and (b) the finite-element-based VFM [16]; (c) the magnitude of the MRI signal [4]. (a)(b)(c) share the same colour bar which is non-dimensional.

References

1. Jérôme F., Mohamed M., Rémi S. and Philippe T. (2006) Detection of small inclusions by elastography. *Inverse Problems* **22**: 1055.
2. Souchon R., Soualmi L., Bertrand M., Chapelon J.Y., Kallel F. and Ophir J. (2002) Ultrasonic elastography using sector scan imaging and a radial compression. *Ultrasonics* **40**: 867-871.
3. Manduca A., Oliphant T.E., Dresner M.A., Mahowald J.L., Kruse S.A., Amromin E., Felmlee J.P., Greenleaf J.F. and Ehman R.L. (2001) Magnetic resonance elastography: Non-invasive mapping of tissue elasticity. *Med Image Anal* **5**: 237-254.
4. Steele D.D., Chenevert T.L., Skovoroda A.R. and Emelianov S.Y. (2000) Three-dimensional static displacement, stimulated echo NMR elasticity imaging. *Phys Med Biol* **45**: 1633-1648.
5. Eunyoung P. and Antoinette M.M. (2006) Shear modulus reconstruction in dynamic elastography: time harmonic case. *Phys Med Biol* **51**: 3697-3721.
6. Doyley M.M., Srinivasan S., Pendergrass S.A., Wu Z. and Ophir J. (2005) Comparative evaluation of strain-based and model-based modulus elastography. *Ultrasound Med Biol* **31**: 787-802.
7. Sacks M.S. (2000) Biaxial mechanical evaluation of planar biological materials. *J Elasticity* **61**: 199-246.
8. Skovoroda A.R., Emelianov S.Y. and Odonnell M. (1995) Tissue elasticity reconstruction based on ultrasonic displacement and strain images. *Ieee T Ultrason Ferr* **42**: 747-765.
9. Barbone P.E. and Gokhale N.H. (2004) Elastic modulus imaging: on the uniqueness and nonuniqueness of the elastography inverse problem in two dimensions. *Inverse Problems* **20**: 283-296.
10. Barbone P.E. and Oberai A.A. (2007) Elastic modulus imaging: some exact solutions of the compressible elastography inverse problem. *Phys Med Biol* **52**: 1577-1593.
11. Sinkus R., Tanter M., Xydeas T., Catheline S., Bercoff J. and Fink M. (2005) Viscoelastic shear properties of in vivo breast lesions measured by MR elastography. *Magn Reson Imaging* **23**: 159-165.
12. Fu D., Levinson S.F., Gracewski S.M. and Parker K.J. (2000) Non-invasive quantitative reconstruction of tissue elasticity using an iterative forward approach. *Phys Med Biol* **45**: 1495-1509.
13. Moussawi A., Lubineau G., Florentin E. and Blaysat B. (2013) The constitutive compatibility method for identification of material parameters based on full-field measurements. *Comput Method Appl M* **265**: 1-14.
14. Pierron F. and Grédiac M. (2012) *The Virtual Fields Methods: Extracting constitutive mechanical parameters from full-field deformation measurements* Springer New-York.
15. Avril S., Grédiac M. and Pierron F. (2004) Sensitivity of the virtual fields method to noisy data. *Comput Mech* **34**: 439-452.
16. Avril S., Huntley J.M., Pierron F. and Steele D.D. (2008) 3D heterogeneous stiffness reconstruction using MRI and the virtual fields method. *Exp Mech* **48**: 479-494.
17. Connesson N., Clayton E.H., Bayly P.V. and Pierron F. (2015) Extension of the optimised virtual fields method to estimate viscoelastic material parameters from 3D dynamic displacement fields. *Strain* **51**: 110-134.
18. Nguyen T.T., Huntley J.M., Ashcroft I.A., Ruiz P.D. and Pierron F. (2014) A Fourier-series-based virtual fields method for the identification of 2-D stiffness distributions. *Int J Numer Meth Eng* **98**: 917-936.

19. Nguyen T.T., Huntley J.M., Ashcroft I.A., Ruiz P.D. and Pierron F. (2014) A Fourier-series-based virtual fields method for the identification of 2-D stiffness and traction distributions. *Strain* **50**: 454-468.
20. Grédiac M., Toussaint E. and Pierron F. (2002) Special virtual fields for the direct determination of material parameters with the virtual fields method. 1 - Principle and definition. *Int J Solids Struct* **39**: 2691-2705.
21. Kim J.H., Pierron F., Wisnom M.R. and Syed-Muhamad K. (2007) Identification of the local stiffness reduction of a damaged composite plate using the virtual fields method. *Compos Part A – Appl S* **38**: 2065-2075.
22. Toussaint E., Grédiac M. and Pierron F. (2006) The virtual fields method with piecewise virtual fields. *Int J Mech Sci* **48**: 256-264.
23. Le Louëdec G., Pierron F., Sutton M.A. and Reynolds A.P. (2013) Identification of the local elasto-plastic behavior of FSW welds using the virtual fields method. *Exp Mech* **53**: 849-859.
24. Sutton M.A., Yan J.H., Avril S., Pierron F. and Adeeb S.M. (2008) Identification of heterogeneous constitutive parameters in a welded specimen: Uniform stress and virtual fields methods for material property estimation. *Exp Mech* **48**: 451-464.
25. Tattoli F., Pierron F., Rotinat R., Casavola C. and Pappalettere C. (2010) Full-field strain measurement on titanium welds and local elasto-plastic identification with the virtual fields method. *Aip Conf Proc* **1315**: 860-865.
26. Nguyen T.T. (2013) The Fourier virtual fields method for the identification of material property distributions. PhD Thesis, Loughborough University (https://dspace.lboro.ac.uk/2134/12658).
27. Hartley R. and Zisserman A. (2003) *Multiple view geometry in computer vision*. 2nd edn. Cambridge University Press, Cambridge, UK ; New York.
28. Sumi C., Suzuki A. and Nakayama K. (1995) Estimation of shear modulus distribution in soft-tissue from strain distribution. *Ieee T Bio-Med Eng* **42**: 193-202.
29. Bersi M.R., Bellini C., Di Achille P., Humphrey J.D., Genovese K. and Avril S. (2016) Novel methodology for characterizing regional variations in the material properties of murine aortas. *J Biomech Eng* **138**: 071015(1–15).
30. Nguyen T.T., Huntley J.M., Ashcroft I.A., Ruiz P.D. and Pierron F. (2014) Fast Fourier virtual fields method for determination of modulus distributions from full-field optical strain data. In: Fringe 2013, W. Osten (Ed). Springer Berlin Heidelberg: 161-166.
31. Erkamp R.Q., Wiggins P., Skovoroda A.R., Emelianov S.Y. and O'Donnell M. (1998) Measuring the elastic modulus of small tissue samples. *Ultrasonic Imaging* **20**: 17-28.
32. Smith J.O. (2003) *Mathematics of the Discrete Fourier Transform (DFT)* W3K Publishing.